minerals

MDPI

Article

Rare Earth Element (REE) Geochemistry of the Cretaceous Tizkuh Formation Limestones, Northwestern Iran: Mineralogical Controls and Paleoenvironmental Implications

Ali Abedini [1,*], Ali Asghar Calagari [2], Nevin Konakci [3] and Ahmet Sasmaz [3]

[1] Department of Geology, Faculty of Sciences, Urmia University, Urmia 57561-51818, Iran
[2] Department of Earth Sciences, Faculty of Natural Sciences, University of Tabriz, Tabriz 51666-16471, Iran; calagari@tabrizu.ac.ir
[3] Department of Geological Engineering, Firat University, 23119 Elazig, Turkey; nevinozturk@firat.edu.tr (N.K.)
* Correspondence: a.abedini@urmia.ac.ir

Abstract

The limestones of the Tizkuh Formation, deposited along the southern margin of the Neo-Tethys Ocean during the Cretaceous, provide an opportunity to investigate REE behavior, depositional processes, and the extent to which primary marine geochemical features may have been retained despite post-depositional modification. In this study, integrated mineralogical (XRD and SEM–EDS) and geochemical (ICP–AES and ICP–MS) data from 15 limestone samples were used to evaluate the controls on major- and trace-element and REE distributions and to assess the preservation of selected marine and redox-related features. The limestones are dominated by calcite, with subordinate kaolinite, quartz, dolomite, illite, hematite, goethite, plagioclase, and locally identified apatite. Negative correlations of CaO with SiO_2, Al_2O_3, TiO_2, Ga, Nb, Zr, Ta, and Th indicate that variations in the relative proportions of carbonate and non-carbonate materials were an important control on whole-rock geochemical variability. Positive associations among Ti, Zr, Nb, Ta, and Ga further support a contribution from siliciclastic materials to the non-carbonate fraction. Total REE concentrations (ΣREE = 31.54–62.18 ppm) are within the range of those commonly reported for marine carbonate rocks and do not indicate anomalous bulk-rock REE enrichment. The positive correlations of ΣREE with Al_2O_3, SiO_2, Th, Zr, Y, and P_2O_5 denote that both siliciclastic and phosphate-bearing components contributed to the bulk-rock REE inventory. The positive relationship between ΣREE and Al_2O_3 (r = 0.55), together with the broadly similar Al-normalized REE patterns among the studied samples, signifies that variations in absolute REE abundances were partly associated with differences in relative proportions of the carbonate and non-carbonate components. However, the consistency of the Al-normalized patterns suggests that the overall REE fractionation pattern cannot be attributed solely to variations in terrigenous dilution. The SEM–EDS data support the occurrence of apatite in the selected samples. The PAAS-normalized REE patterns show limited LREE enrichment relative to HREE, indicating that the REE system does not represent an unmodified seawater signature and was influenced by the non-carbonate components and post-depositional processes. Weak negative Ce anomalies (Ce/Ce* = 0.76–0.94), together with Pr/Pr* values close to unity and relatively low U/Th (0.04–0.11) and V/Cr (0.77–1.90) ratios, are compatible with relatively oxidizing marine depositional conditions. However, the preservation of a primary seawater Ce signal remains tentative because Ce/Ce* is associated with the non-carbonate and REE-bearing components, while U and V may be affected by diagenetic redistribution and other post-depositional processes. Positive Eu anomalies (Eu/Eu* = 1.44–1.98) are interpreted cautiously and may reflect a combination

Check for updates

Academic Editor: Hao Tang

Received: 4 August 2026
Revised: 1 September 2026
Accepted: 2 September 2026
Published: 4 September 2026

Copyright: © 2026 by the authors. Licensee MDPI, Basel, Switzerland. This article is an open access article distributed under the terms and conditions of the Creative Commons Attribution (CC BY) license.

of mineralogical controls, limited detrital feldspar contribution, and possible early diagenetic and/or fluid–rock interaction. Overall, the Tizkuh limestones represent a mixed and partially modified carbonate geochemical archive in which selected depositional and redox-related features may have been retained. Consequently, reconstruction of the Cretaceous paleoenvironment requires a multi-proxy approach integrating REE patterns, Ce and Eu anomalies, Y/Ho ratios, U/Th, V/Cr, detrital and phosphate indicators, Al-normalized REE patterns, geochemical relationships, and mineralogical evidence.

Keywords: Tizkuh Formation; limestone; REE; carbonate dilution; diagenesis; paleoenvironment; Cretaceous

1. Introduction

Carbonate rocks as one of the very valuable geological archives have been known for the reconstruction of paleo-climatic and paleoenvironmental conditions of the Earth [1–4]. This is because carbonate sediments are commonly formed in close interaction with seawater and may incorporate geochemical information during deposition and early diagenesis. They can also preserve useful evidence of depositional conditions, seawater chemistry, redox state, and post-depositional processes [5–7]. However, the extent of preservation depends strongly on recrystallization, terrigenous input, phosphate phases, and other diagenetic processes. In addition, variations in the relative proportions of carbonate and non-carbonate components may modify bulk-rock rare earth elements (REE) values through dilution or concentration effects, potentially obscuring the primary distribution patterns of REE. For this reason, in recent decades carbonate successions have been widely used for investigations of paleo-oceanology and reconstruction of depositional environments [5–10]. Among various geochemical proxies, REE due to their regular geochemical behaviors can play a significant role in the analysis of depositional conditions and post-depositional processes [11–13]. These elements owing to the similarity of their electron configurations and smooth change in ionic radii in lanthanide series can portray clear-cut distribution patterns for marine environments and also provide unique information on seawater chemistry, redox (Eh) conditions, rate of terrigenous input to depositional environment, influence of hydrothermal fluids, and intensity of diagenetic processes for limestones [14–17].

Distribution patterns of lanthanides in modern seawaters show an enrichment of the heavy REE (HREE) relative to light REE (LREE), high Y/Ho ratios, and negative Ce anomalies [18–20]. These characteristics may be transferred to carbonate sediments during deposition and, if sufficiently preserved, can provide useful means to constrain the chemical conditions of paleo-seawater. Nevertheless, their preservation should be evaluated against potential detrital, phosphate, and diagenetic overprints [14,21–24]. In particular, the contribution of terrigenous material needs to be distinguished from the marine component because aluminosilicate-rich detrital phases may contribute REE to bulk carbonate samples and may also alter apparent REE abundances through dilution or concentration effects. Accordingly, normalization of REE concentrations to an element associated predominantly with the terrigenous fraction, such as Al, can provide an additional means of evaluating the extent to which variations in REE abundances are related to changes in non-carbonate input. For this reason, certain geochemical parameters affiliated to with REE such as Ce/Ce*, Eu/Eu*, $(La/Yb)_N$, and $(Nd/Yb)_N$ can be broadly utilized for recognition of the primary signatures of seawater and their separation from secondary effects such as diagenesis [16,25–28].

Among these indices, Ce and Eu anomalies are particularly significant in investigations of depositional environments. Cerium is the only lanthanide element that, under oxidizing conditions, changes its oxidation state from Ce^{3+} to Ce^{4+} and exits from the

seawater column. Because of this unique geochemical characteristic, negative Ce anomalies are widely used as an indicator of relatively oxidizing conditions in marine environments, although their interpretation in ancient carbonates requires the consideration of possible diagenetic and detrital influences [1,29,30]. By contrast, positive Eu anomaly can present precious information about the influence of hydrothermal fluids, reduced Eh conditions of the precipitation environment, temperature increment, and water–rock interaction during diagenetic processes [31,32]. In other words, positive Eu anomalies are not uniquely diagnostic of any single process but rather they may be influenced by mineralogical composition, detrital feldspar, and post-depositional fluid–rock interaction. Therefore, simultaneous examination of Ce and Eu anomalies can provide worthwhile information concerning conditions of the depositional environment and diagenetic case history of limestones [33–37]. Despite widespread application of REE in investigation of limestones, analysis of REE distribution patterns is always accompanied by certain challenges. Processes such as recrystallization of calcite, dissolution, cementation, the existence of phosphate and Fe–Mn oxide minerals, and terrigenous input can influence the amount of REE and even their distribution pattern [16]. Consequently, the interpretation of REE patterns in ancient carbonates requires an integrated assessment of absolute REE abundances, normalized REE distributions, and their relationships with terrigenous- and phosphate-associated elements rather than reliance on individual REE anomalies alone.

The Cretaceous time is reckoned to be one of the most important geologic periods in view of evolution of oceanic systems and precipitation of carbonate rocks. The prominent characteristics of this geologic period are the global high seawater level, the greenhouse conditions prevailing over the Earth's climate, and vast spread of carbonate platforms worldwide [38–40]. In this period, the Neo-Tethys Ocean used to cover a large part of Iran and hence widespread carbonate sediments were deposited, which nowadays can be reckoned to be one of the most significant sources of information for paleoenvironments [41]. The Tizkuh Formation is one of the important carbonate units of Cretaceous age in the Central Zone of Iran which was precipitated in the southern margin of the Neo-Tethys Ocean and has special importance in view of stratigraphy, sedimentology, and evolution of sedimentary basins. No investigations on geochemical features of REE in the limestones of the Tizkuh Formation and the capability of these elements in recording geochemical signatures of ancient seawater have been carried out as yet. Moreover, the extent to which variations in terrigenous and phosphate-bearing components influence bulk-rock REE abundances, and whether the observed REE fractionation patterns persist after accounting for the terrigenous component, have not been evaluated. Moreover, consideration of diagenetic processes and terrigenous input in controlling the behavior of lanthanides and the measure of their effects on reconstruction of geochemical conditions of the Cretaceous seawater still demands more meticulous examination. Thus, in this research, it is endeavored to consider the mineralogical and geochemical characteristics of REE in the limestones of the Tizkuh Formation in northwestern Iran.

Distinctively, the main objectives of the current study are (1) consideration of distribution patterns of REE in the limestones, (2) assessment of the extent to which selected primary marine and redox-related features may have been retained using Ce and Eu anomalies and other geochemical indices, (3) investigation of the role of diagenetic processes and terrigenous input in controlling REE behavior, including evaluation of potential dilution or concentration effects associated with variations in the non-carbonate fraction, and (4) assessment of conditions of the paleoenvironment and the redox state prevailing over the sedimentary environment during deposition of the limestones. The conclusions of this research can remarkably help in better understanding the conditions of geochemical evolution of the Neo-Tethys basin during the Cretaceous.

2. Geological Setting

The Amir–Abad area is located south of Maragheh city in East Azarbaidjan Province, NW Iran. According to the structural zoning of Iran [42], the study area is situated within the Central Iran structural zone (Figure 1a). This region occupies a tectonically important setting within the Iranian sector of the Neo-Tethyan domain and records a complex history of Paleozoic–Mesozoic sedimentation associated with the opening, evolution, and subsequent closure of the Neo-Tethys Ocean [43,44]. During the Mesozoic, variations in the configuration of the Neo-Tethyan oceanic domain and its adjacent continental margins provided conditions for the development of shallow-marine sedimentary basins and carbonate platforms across different parts of Iran. In the Central Iran structural zone, Cretaceous marine transgression and the development of relatively shallow-marine environments resulted in widespread deposition of carbonate successions [43,45]. The Tizkuh Formation represents part of this Cretaceous carbonate succession and records carbonate-platform sedimentation along the Iranian sector of the Neo-Tethyan realm.

The geologic outcrops of the Amir–Abad area encompass successions of lithologic units from Permian to Quaternary (Figure 1b). The oldest rock units exposed in the area belong to carbonates of the Ruteh Formation (Permian) and dolomites of the Elika Formation (Triassic) (see Figure 1b) [13]. A bauxitic horizon overlies the Elika Formation, which is in turn conformably overlain by the Shemshak Formation (Lower Jurassic), consisting principally of sandstone, siltstone, coal-bearing horizons, and locally basaltic rocks, recording a mixed continental to shallow-marine depositional succession with associated volcanic activity. This formation is also conformably overlain by marly limestones of the Dalichay Formation (Middle Jurassic) and limestones and dolomitic limestones of the Lar Formation (Upper Jurassic), indicating the development of a relatively stable carbonate platform during the Late Jurassic. These siliciclastic and volcanic units prepared a regional geologic ground for potential non-carbonate input to the overlying carbonate succession, although their specific contribution to the studied limestones has been evaluated on the basis of mineralogical and geochemical evidence rather than being inferred solely from stratigraphic relationships.

The Cretaceous succession exposed in the Amir–Abad area can be broadly divided into a lower volcanic interval dominated by basic volcanic rocks, mainly basalt, and an overlying carbonate-dominated interval represented by the Tizkuh Formation. In the studied profile, the Tizkuh Formation forms an approximately 440 m thick carbonate succession overlying the basaltic rocks. The carbonate beds are broadly parallel to the underlying volcanic rocks at the observed contact, which is therefore described conservatively as a subparallel basalt–limestone contact. Because no systematic evidence for angular discordance, erosional relief, paleosol development, or the duration of a stratigraphic hiatus was documented during the present field investigation, the contact is not classified here as a specific type of unconformity, such as a nonconformity or disconformity.

The Tizkuh Formation is predominantly composed of limestone and dolomitic limestone, with systematic variations in bed thickness throughout the succession. The lower and upper parts are mainly characterized by thin- to medium-bedded limestones, whereas the middle part is dominated by medium- to thick-bedded limestones. The carbonate beds are generally light gray to creamy in color, regularly bedded, and laterally continuous at the outcrop scale. Chert occurs locally within the limestone succession as bands, lenses, and nodules, and its abundance varies in each individual bed. These lithological variations are readily recognizable in the field and provide an important basis for distinguishing the principal carbonate intervals within the studied succession. The analyzed samples were collected from representative limestone beds, and their selection was based on the principal lithological variability observed along the exposed carbonate succession. This sampling strategy provides coverage of the principal lithological variation within

the exposed carbonate succession, allowing variations in the relative proportions of the carbonate and non-carbonate components to be considered when evaluating whole-rock geochemical variability.

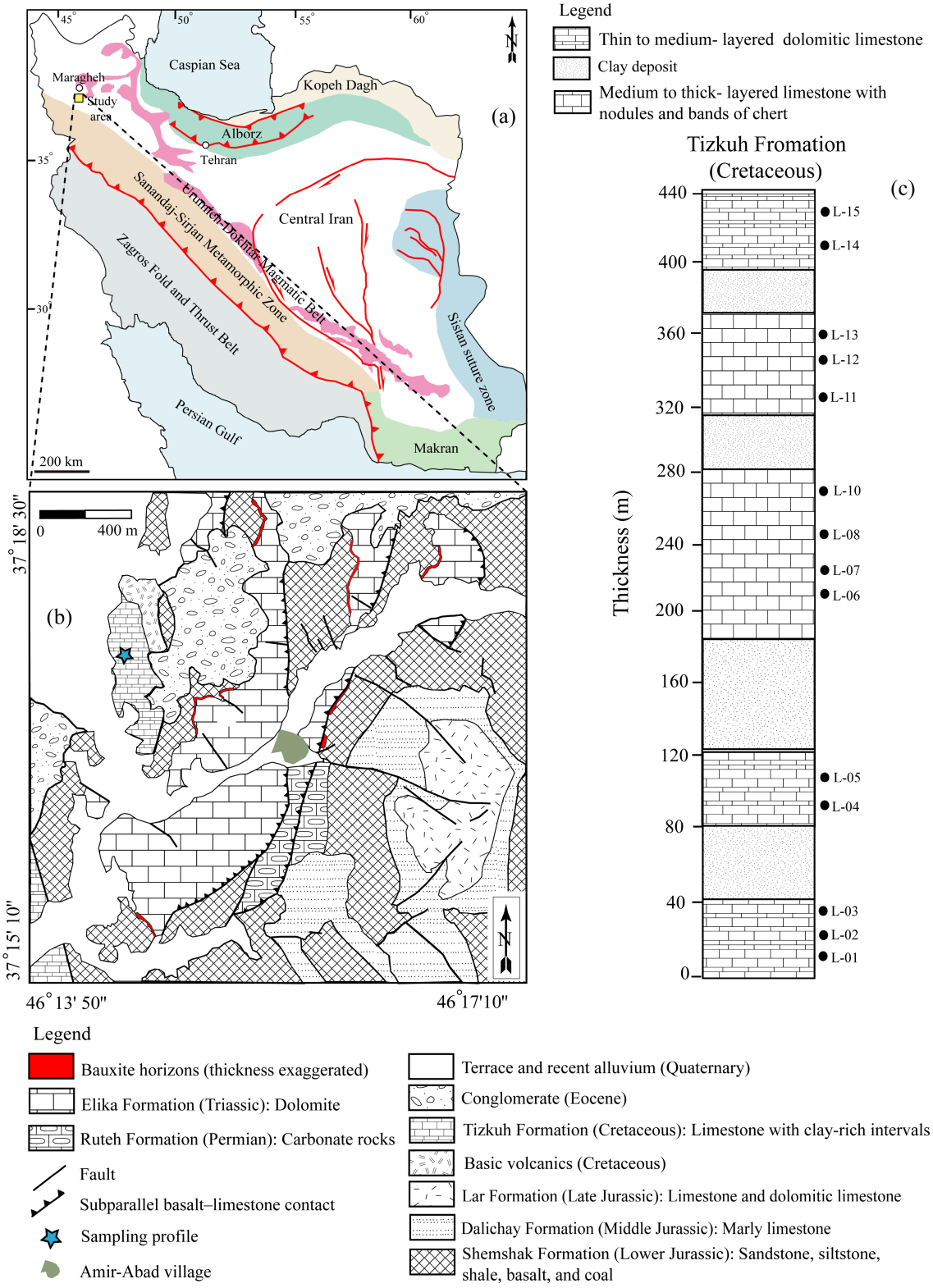


Figure 1. (**a**) Structural map of Iran [42], showing the position of the study area (Amir–Abad) in the Central Iran structural zone. (**b**) Geologic map of the Amir–Abad area [13], showing the position of the sampling profile in the Tizkuh Formation by an asterisk. (**c**) The sampling profile, showing the positions of the collected limestone samples with filled circles.

The stratigraphic consideration of the studied interval as belonging to the Tizkuh Formation is based primarily on its lithological characteristics and regional stratigraphic relationships. No independent new biostratigraphic dataset was generated in the present study; therefore, the study does not attempt to establish a high-resolution biostratigraphic framework for the 440 m thick succession. The well-exposed and laterally continuous carbonate beds, together with the preservation of their primary lithological characteristics, provide a suitable field framework for the mineralogical and geochemical investigation of the Cretaceous limestones. The youngest lithologic units in the study area belong to the Eocene conglomerate and Quaternary alluvial sediments (see Figure 1b).

3. Method of Investigation

A total of 15 relatively fresh limestone samples, showing little or no evidence of surface weathering, were collected from selected stratigraphic and lithological intervals along the profile (Figure 1c). Fresh materials were preferentially collected from the unweathered interior of the beds, away from exposed surfaces, fractures, veins, obvious discoloration, and zones showing visible alteration or secondary mineral growth. Thin sections were prepared from all 15 samples and examined under a polarizing microscope to characterize their petrographic features and identify carbonate and non-carbonate mineral phases, as well as evidence of recrystallization and other post-depositional features. The sampling strategy was designed to cover the principal limestone horizons and lithological variations recognized within the exposed section rather than to achieve uniform systematic sampling at a fixed vertical interval. Accordingly, the selected samples provide a representative dataset for evaluating the major mineralogical and geochemical characteristics of the sampled limestone intervals, but are not intended to resolve continuous high-resolution vertical variations throughout the entire 440 m thick succession.

After sampling, the rock specimens were crushed and then milled to a grain size of <75 μm. For determination of the mineralogical composition and semi-quantitative relative abundances of the identified mineral phases in all 15 limestone samples, X-ray diffraction (XRD) analyses were performed using a Siemens D5000 diffractometer at the XRD Laboratory of the Geological Survey of Iran (GSI). The analyses were conducted using Cu-Kα radiation (λ = 1.5406 Å), at 40 kV and 30 mA, over a 2–70° 2θ scanning range, with a step size of 0.02° and a scanning speed of 1° min^{-1}. The diffraction patterns were identified using the ICDD (International Center for Diffraction Data) database. The relative abundances of the major rock-forming minerals were estimated following the approach of Brindley [46], based on the relative intensities of diagnostic XRD reflections and corresponding intensity factors, whereas the relative abundances of the clay minerals were determined from their basal reflections and intensity factors following Moore and Reynolds [47]. The resulting mineralogical data are presented in Table 1 as semi-quantitative relative abundance classes. The number of "+" symbols reflects progressively increasing relative abundance of the corresponding mineral phase, whereas "acc" denotes an accessory occurrence. These values represent relative estimates rather than absolute mineral percentages.

Additionally, for complementary mineralogical characterization at the microscale, two selected samples were examined using scanning electron microscopy coupled with energy-dispersive X-ray spectrometry (SEM–EDS) at the Razi Metallurgical Research Center (Iran). The analyses were conducted using an accelerating voltage of 15 kV, a beam current of 1 nA, and a beam diameter of 1 μm. The two samples were selected to provide complementary microscale evidence for the mineralogical characteristics identified by XRD and petrographic examination. Representative SEM images and corresponding EDS spectra were used for the qualitative identification of calcite, kaolinite, and apatite based on their characteristic elemental signatures. The EDS results are presented as qualitative

mineral-identification evidence rather than quantitative or semi-quantitative compositional data. Accordingly, the SEM–EDS observations are considered supportive evidence for the occurrence of these phases in the two analyzed samples and are not generalized to the entire succession.

Table 1. Mineralogical composition and semi-quantitative relative abundances of the studied limestones of the Tizkuh Formation in the Amir–Abad area. Cal: calcite; Kln: kaolinite; Dol: dolomite; Ilt: illite; Qz: quartz; Hem: hematite; Gth: goethite; Pl: plagioclase; acc: accessory occurrence. The number of "+" symbols reflects progressively increasing relative abundance of the corresponding mineral phase based on the intensity of its diagnostic XRD reflections. The reported abundances are semi-quantitative relative estimates and do not represent absolute mineral percentages.

	Cal	Kln	Dol	Ilt	Qz	Hem	Gth	Pl
L-01	+++++	++	+	+	++	+		
L-02	+++++	++	+	+	++	acc		
L-03	++++++	++	+		++			
L-04	+++++	++		+	+	acc		acc
L-05	+++++	++		+	++			
L-06	+++++	++		+	++			
L-07	++++++	++	acc		+	acc		
L-08	++++++	++	acc		++			
L-09	++++++	++		+	++	acc		
L-10	++++++	++	acc		++			
L-11	++++++	++	+		+		acc	
L-12	+++++	++	acc		++		acc	
L-13	+++++	++		+	++			acc
L-14	+++++	++	acc	+	++			
L-015	++++++	++	+		++			

For determination of the chemical composition of the samples, major elements were analyzed by inductively coupled plasma atomic emission spectrometry (ICP–AES), whereas trace elements, including REEs, were analyzed by inductively coupled plasma mass spectrometry (ICP–MS) at ALS Chemex Laboratories, Vancouver, Canada. Prior to analysis, the powdered samples were subjected to the laboratory's acid-digestion procedure. Analytical quality control included the analysis of certified reference materials (CRMs), duplicate samples, and procedural blanks as part of the laboratory's routine quality-control procedures. CRMs were used to monitor analytical accuracy, duplicate analyses were used to evaluate analytical reproducibility, and procedural blanks were used to monitor potential contamination during sample preparation and analysis. The reported detection limits were approximately 0.01 wt% for major elements, 0.1–20 ppm for trace elements, and 0.01–0.1 ppm for REE, depending on the element and analytical method. Detailed information on the specific CRM identities, element-specific recovery values, duplicate deviations, blank concentrations, and analytical uncertainties was not included in the analytical report available to the authors; therefore, these parameters are not quantitatively reported here. This limitation has been explicitly acknowledged to avoid introducing undocumented analytical values. The values of LOI (loss on ignition) were obtained by measuring the weight loss of 1 g of each specimen after heating at 950 °C for 90 min. The complete results of the chemical analyses are listed in Table 2.

Table 2. Quantitative concentrations of major and trace elements in the studied limestone samples from Amir–Abad, measured using ICP–AES and ICP–MS methods.

	L-01	**L-02**	**L-03**	**L-04**	**L-05**	**L-06**	**L-07**	**L-08**	**L-09**	**L-10**	**L-11**	**L-12**	**L-13**	**L-14**	**L-15**	**Min**	**Max**	**Ave**	**Stdev**
SiO_2 (wt%)	16.35	14.88	12.96	15.25	16.04	15.21	12.62	14.15	14.73	13.33	12.81	13.62	14.49	15.26	12.85	12.62	16.35	14.30	1.22
Al_2O_3	5.79	5.36	4.57	6.06	5.61	5.63	4.36	4.78	5.25	4.78	4.41	4.95	5.66	5.41	4.65	4.36	6.06	5.15	0.54
Fe_2O_3	2.03	2.02	1.86	2.03	1.99	1.92	1.93	1.95	1.83	1.82	2.01	1.91	1.87	1.89	1.89	1.82	2.03	1.93	0.07
CaO	38.26	35.58	42.66	36.89	37.25	39.58	42.36	41.74	40.15	41.54	42.52	39.76	38.33	39.04	41.21	35.58	42.66	39.79	2.22
MgO	0.81	0.83	0.82	0.77	0.75	0.78	0.82	0.84	0.74	0.85	0.81	0.79	0.77	0.79	0.82	0.74	0.85	0.80	0.03
Na_2O	0.14	0.16	0.14	0.27	0.21	0.11	0.09	0.15	0.11	0.15	0.09	0.18	0.23	0.21	0.16	0.09	0.27	0.16	0.05
K_2O	0.68	0.66	0.62	0.74	0.64	0.66	0.59	0.55	0.65	0.63	0.62	0.58	0.71	0.63	0.58	0.55	0.74	0.64	0.05
TiO_2	0.12	0.11	0.08	0.14	0.13	0.11	0.07	0.09	0.11	0.08	0.06	0.10	0.12	0.11	0.09	0.06	0.14	0.10	0.02
MnO	0.02	0.01	0.02	0.02	0.01	0.02	0.03	0.03	0.03	0.02	0.02	0.02	0.02	0.03	0.03	0.01	0.03	0.02	0.01
P_2O_5	0.15	0.13	0.11	0.12	0.16	0.14	0.10	0.14	0.15	0.11	0.09	0.12	0.11	0.11	0.10	0.09	0.16	0.12	0.02
LOI	35.64	40.19	36.08	37.69	37.05	35.65	36.75	35.24	36.01	36.41	36.52	37.95	37.48	36.51	37.55	35.24	40.19	36.85	1.23
Sum	99.99	99.93	99.92	99.98	99.84	99.81	99.72	99.66	99.76	99.72	99.96	99.98	99.79	99.99	99.93	99.66	99.99	99.87	0.11
V (ppm)	23	20	19	26	22	23	19	18	22	19	20	19	25	23	21	18	26	21	2
Cr	30	24	10	25	26	22	22	18	15	10	23	18	18	19	14	10	30	20	6
Co	3.8	2.9	4.9	3.1	3.6	3.7	4.7	3.8	3.6	3.7	4.7	3.6	3.6	3.5	4.2	2.9	4.9	3.8	0.6
Ga	12.7	11.6	9.9	13.6	12.1	12.5	9.9	10.6	11.5	10.3	9.5	10.6	12.3	11.6	10.1	9.5	13.6	11.3	1.2
Ta	3.8	3.5	2.9	4.1	3.5	3.8	2.8	3.2	3.6	3.2	2.9	3.2	3.6	3.4	3.2	2.8	4.1	3.4	0.4
Cs	4.53	3.62	2.72	4.85	4.02	4.25	2.22	2.23	3.75	3.15	2.32	2.49	4.21	3.85	2.26	2.22	4.85	3.36	0.93
Ni	17	16	21	19	17	20	22	20	18	22	23	19	20	21	22	16	23	20	2
Rb	8.2	6.6	4.9	8.8	7.3	7.7	4.0	3.4	6.8	5.7	4.2	4.5	7.6	7.0	4.1	3.4	8.8	6.0	1.7
Ba	16.2	15.5	14.6	17.3	15.1	16.2	14.2	13.5	15.7	14.9	14.6	13.6	16.3	14.3	14.6	13.5	17.3	15.1	1.1
Sr	215.3	147.6	261.2	195.4	162.8	208.5	229.3	240.1	238.5	234.2	229.3	234.6	194.9	235.1	233.6	147.6	261.2	217.4	30.8
Th	8.54	7.93	7.41	8.05	9.67	10.09	7.15	9.62	9.45	7.68	7.23	7.65	9.41	8.02	8.54	7.15	10.09	8.43	0.99
U	0.83	0.61	0.42	0.91	0.58	0.65	0.41	0.48	0.63	0.41	0.42	0.49	0.62	0.66	0.38	0.38	0.91	0.57	0.16
Cu	12	8	24	11	14	20	23	25	18	20	21	18	15	19	23	8	25	18	5
Y	5.2	4.6	4.3	4.3	5.8	5.7	4.2	5.3	6.5	4.3	4.3	4.7	5.0	4.9	4.8	4.2	6.5	4.9	0.7
Zr	40	37	23	32	41	34	21	37	36	24	25	29	30	29	27	21	41	31	6
Pb	19	17	21	18	19	20	21	20	20	21	21	19	19	18	21	17	21	20	1
Zn	35	28	21	33	28	28	24	31	21	23	33	26	21	24	25	21	35	27	5
Nb	3.6	2.6	1.8	4.1	3.6	3.5	1.8	2.0	2.8	1.8	1.8	2.8	3.3	3.1	2.3	1.8	4.1	2.7	0.8
Hf	8.8	7.8	5.7	9.4	8.9	5.6	5.9	6.3	5.2	5.6	7.9	7.7	6.5	5.1	6.8	5.1	9.4	6.9	1.4
La	13.6	10.9	8.3	9.2	14.9	12.4	7.6	11.3	12.5	8.6	8.2	8.7	9.0	8.8	8.5	7.6	14.9	10.2	2.3

Table 2. *Cont.*

	L-01	L-02	L-03	L-04	L-05	L-06	L-07	L-08	L-09	L-10	L-11	L-12	L-13	L-14	L-15	Min	Max	Ave	Stdev
Ce	22.6	18.2	13.5	14.6	26.8	22.3	11.9	20.6	23.1	13.8	13.9	13.7	15.8	14.3	14.6	11.9	26.8	17.3	4.6
Pr	2.63	2.25	1.81	2.01	2.86	2.53	1.72	2.36	2.57	1.85	1.80	1.87	1.94	1.90	1.84	1.72	2.86	2.13	0.37
Nd	10.1	7.9	6.4	7.3	10.8	8.4	6.2	8.1	8.6	6.5	6.4	6.8	7.0	6.9	6.6	6.2	10.8	7.6	1.4
Sm	1.66	1.45	1.18	1.26	1.76	1.50	1.09	1.49	1.54	1.21	1.14	1.18	1.22	1.20	1.18	1.09	1.76	1.34	0.21
Eu	0.52	0.46	0.39	0.38	0.63	0.58	0.31	0.54	0.62	0.35	0.35	0.36	0.43	0.39	0.41	0.31	0.63	0.45	0.10
Gd	1.26	1.14	1.03	1.05	1.34	1.32	0.93	1.16	1.38	1.06	0.96	0.99	1.02	1.01	1.01	0.93	1.38	1.11	0.15
Tb	0.17	0.15	0.13	0.14	0.19	0.17	0.12	0.16	0.18	0.14	0.13	0.13	0.14	0.13	0.13	0.12	0.19	0.15	0.02
Dy	0.94	0.84	0.74	0.75	1.09	0.99	0.69	0.85	1.06	0.79	0.71	0.72	0.74	0.73	0.73	0.69	1.09	0.82	0.13
Ho	0.21	0.19	0.16	0.17	0.24	0.23	0.15	0.20	0.24	0.18	0.16	0.16	0.17	0.16	0.16	0.15	0.24	0.19	0.03
Er	0.57	0.51	0.43	0.46	0.68	0.65	0.39	0.53	0.68	0.51	0.41	0.43	0.44	0.43	0.43	0.39	0.68	0.50	0.10
Tm	0.08	0.07	0.06	0.06	0.10	0.09	0.05	0.07	0.09	0.07	0.05	0.06	0.06	0.06	0.06	0.05	0.1	0.07	0.02
Yb	0.53	0.48	0.39	0.41	0.69	0.61	0.34	0.48	0.63	0.47	0.36	0.38	0.39	0.38	0.38	0.34	0.69	0.46	0.11
Lu	0.08	0.07	0.06	0.06	0.10	0.09	0.05	0.07	0.10	0.07	0.05	0.06	0.06	0.06	0.06	0.05	0.10	0.07	0.02

https://doi.org/10.3390/min16090914

For analysis of lanthanide behavior, the REE concentrations were normalized to the Post-Archean Australian Shale (PAAS) composition reported by Taylor and McLennan [28]. The PAAS reference composition [28] was consistently applied to all normalized REE concentrations, ratios, and anomaly calculations presented in this study. To further evaluate the influence of variations in the aluminosilicate-rich terrigenous component on bulk-rock REE distributions, the measured REE concentrations were also evaluated relative to Al_2O_3. Al_2O_3 was used as a proxy for the aluminosilicate-rich non-carbonate component because of its associations with SiO_2 and several lithophile elements in the studied samples. REE/Al_2O_3 ratios were calculated using the measured concentrations of individual REEs and the corresponding Al_2O_3 contents. The resulting Al_2O_3-normalized REE patterns were used as a complementary approach to assess the consistency of REE distributions relative to variations in the non-carbonate fraction and to distinguish changes in absolute REE abundances from changes in REE fractionation. Moreover, several indices and geochemical ratios, including CaO/MgO, Mn/Sr, Ba/Nd, Ba/Sm, Y/Ho, ΣREE, ΣLREE, ΣHREE, Er/Nd, $(La/Yb)_N$, $(La/Sm)_N$, $(Nd/Yb)_N$, Ce/Ce*, Eu/Eu*, Pr/Pr*, V/Cr, and U/Th, were calculated, and their values and calculation procedures are presented in Table 3. The U/Th ratio was used as a supporting redox indicator and was interpreted cautiously because U may be mobile during post-depositional alteration. The Ce, Eu, and Pr anomalies were calculated using the following equations:

$$Ce/Ce^* = 2Ce_N/(La_N + Pr_N)$$

$$Eu/Eu^* = 2Eu_N/(Sm_N + Gd_N)$$

$$Pr/Pr^* = 2Pr_N/(Ce_N + Nd_N)$$

where the subscript N denotes normalization to PAAS. The normalized REE ratios, including $(La/Sm)_N$ and $(Nd/Yb)_N$, were calculated from the corresponding PAAS-normalized concentrations.

To evaluate relationships among the analyzed elements, Pearson correlation coefficients were calculated (Table 4). Given the relatively small sample size (n = 15), the statistical significance of the correlations was assessed using two-tailed tests and is indicated by one and two asterisks in Table 4 for $p < 0.05$ and $p < 0.01$, respectively. Because major-element data are compositional and may be affected by closed-sum effects, the correlation coefficients were interpreted cautiously and in conjunction with mineralogical and other geochemical evidence rather than as direct evidence of causal relationships or specific mineral hosts. In particular, the relationships between ΣREE and Al_2O_3 were evaluated as complementary evidence for assessing the influence of variations in the non-carbonate component on bulk-rock REE concentrations. The geochemical ratios and relevant discrimination diagrams were used to evaluate REE behavior, terrigenous and phosphate contributions, the extent of diagenetic modification, and the degree to which primary marine and redox-related signatures may have been preserved or modified.

Table 3. Values of selected geochemical parameters calculated for the samples collected from the limestones in the Amir–Abad area.

	L-01	L-02	L-03	L-04	L-05	L-06	L-07	L-08	L-09	L-10
CaO/MgO	47.23	42.87	52.02	47.91	49.67	50.74	51.66	49.69	54.26	48.87
Mn/Sr	0.72	0.52	0.59	0.79	0.48	0.74	1.01	0.97	0.97	0.66
Ba/Nd	1.60	1.96	2.28	2.37	1.40	1.93	2.29	1.67	1.83	2.29
Ba/Sm	9.76	10.69	12.37	13.73	8.58	10.80	13.03	9.06	10.19	12.31
U/Th	0.10	0.08	0.06	0.11	0.06	0.06	0.06	0.05	0.07	0.05
V/Cr	0.77	0.83	1.90	1.04	0.85	1.05	0.86	1.00	1.47	1.90
Y/Ho	24.76	24.21	26.88	25.29	24.17	24.78	27.67	26.50	27.08	23.89
LREE	51.11	41.15	31.58	34.75	57.75	47.71	28.82	44.39	48.89	32.30
HREE	3.84	3.45	3.00	3.10	4.43	4.15	2.72	3.52	4.36	3.29
REE	54.95	44.60	34.58	37.85	62.18	51.86	31.54	47.91	53.25	35.59
Er/Nd	0.06	0.06	0.07	0.06	0.06	0.08	0.06	0.07	0.08	0.08
$(La/Yb)_N$	1.89	1.67	1.57	1.65	1.59	1.50	1.65	1.73	1.46	1.35
$(La/Sm)_N$	1.21	1.11	1.04	1.08	1.25	1.22	1.03	1.12	1.19	1.05
$(Nd/Yb)_N$	1.67	1.44	1.44	1.56	1.37	1.20	1.60	1.48	1.19	1.21
Ce/Ce*	0.86	0.84	0.80	0.78	0.94	0.91	0.76	0.92	0.94	0.80
Pr/Pr*	0.99	1.06	1.10	1.10	0.96	1.05	1.13	1.04	1.04	1.10
Eu/Eu*	1.67	1.67	1.65	1.54	1.91	1.92	1.44	1.91	1.98	1.44

	L-11	L-12	L-13	L-14	L-15	Min	Max	Ave	Stdev
CaO/MgO	52.49	50.33	49.78	49.42	50.26	42.87	54.26	49.81	2.62
Mn/Sr	0.68	0.66	0.79	0.99	0.99	0.48	1.01	0.77	0.18
Ba/Nd	2.28	2.00	2.33	2.07	2.21	2.18	1.40	2.37	0.29
Ba/Sm	12.81	11.53	13.36	11.92	12.37	12.39	8.58	13.73	1.55
U/Th	0.06	0.06	0.07	0.08	0.04	0.04	0.11	0.07	0.02
V/Cr	0.87	1.06	1.39	1.21	1.50	0.77	1.90	1.18	0.37
Y/Ho	27.48	29.53	30.38	29.96	30.00	23.89	30.38	26.84	2.31
LREE	31.83	32.55	35.41	33.48	33.10	28.82	57.75	38.99	8.86
HREE	2.82	2.91	3.01	2.96	2.96	2.72	4.43	3.37	0.57
REE	34.65	35.46	38.42	36.43	36.05	31.54	62.18	42.35	9.40
Er/Nd	0.06	0.06	0.06	0.06	0.07	0.06	0.08	0.07	0.01
$(La/Yb)_N$	1.68	1.69	1.70	1.71	1.65	1.35	1.89	1.63	0.13
$(La/Sm)_N$	1.06	1.09	1.09	1.08	1.07	1.03	1.25	1.11	0.07
$(Nd/Yb)_N$	1.58	1.57	1.57	1.57	1.50	1.19	1.67	1.46	0.16
Ce/Ce*	0.83	0.78	0.87	0.80	0.85	0.76	0.94	0.85	0.06
Pr/Pr*	1.08	1.10	1.04	1.08	1.06	0.96	1.13	1.06	0.04
Eu/Eu*	1.56	1.56	1.80	1.66	1.76	1.44	1.98	1.70	0.18

Note: Post-Archean Australian Shale (PAAS)-normalized data are from McLennan [28]; the subscript N denotes normalization of lanthanides to PAAS; LREE = La + Ce + Pr + Nd + Sm + Eu; HREE = Gd + Tb + Dy + Ho + Er + Tm + Yb + Lu; REE = La + Ce + Pr + Nd + Sm + Eu + Gd + Tb + Dy + Ho + Er + Tm + Yb + Lu; $(La/Sm)_N$: La and Sm are normalized to PAAS; $(Nd/Yb)_N$: Nd and Yb are normalized to PAAS; the values of Ce/Ce*, Pr/Pr*, and Eu/Eu* represent the respective PAAS-normalized results; $Ce/Ce^* = 2Ce_N/(La_N + Pr_N)$ [28]; $Eu/Eu^* = 2Eu_N/(Sm_N + Gd_N)$ [47]; $Pr/Pr^* = 2Pr_N/(Ce_N + Nd_N)$ [3,16,30].

Table 4. Pearson correlation coefficients between major and trace elements in the studied limestone samples collected from the Amir–Abad area. Statistical significance was evaluated using two-tailed tests; * and ** indicate significance at $p < 0.05$ and $p < 0.01$, respectively.

	Si	Al	Fe	Ca	Mg	Na	K	Ti	P	V	Cr	Co	Ga	Ta	Cs
Si	1.00														
Al	0.91 **	1.00													
Fe	0.41	0.34	1.00												
Ca	−0.79 **	−0.86 **	−0.48	1.00											
Mg	−0.52 *	−0.59 *	0.01	0.43	1.00										
Na	0.44	0.63 *	0.14	−0.63 *	−0.34	1.00									
K	0.59 *	0.80 **	0.26	−0.67 **	−0.49	0.49	1.00								
Ti	0.87 **	0.96 **	0.29	−0.87 **	−0.65 *	0.72 **	0.69 **	1.00							
P	0.78 **	0.59 *	0.22	−0.50	−0.43	0.08	0.20	0.63 *	1.00						
V	0.64	0.84 **	0.20	−0.62 *	−0.67 **	0.60 *	0.85 **	0.78 **	0.20	1.00					
Cr	0.63 *	0.54 *	0.88 **	−0.59 *	−0.27	0.13	0.39	0.46	0.39	0.42	1.00				
Co	−0.69 **	−0.76 **	−0.22	0.85 **	0.31	−0.60 *	−0.49	−0.78 **	−0.50	−0.47	−0.31	1.00			
Ga	0.88 **	0.99 **	0.37	−0.82 **	−0.58 *	0.60 *	0.81 **	0.94 **	0.58 *	0.85 **	0.57 *	−0.73 **	1.00		
Ta	0.83 **	0.96 **	0.30	−0.78 **	−0.54 *	0.53 *	0.78 **	0.91 **	0.58 *	0.82 **	0.47	−0.77 **	0.96 **	1.00	
Cs	0.86 **	0.96 **	0.25	−0.77 **	−0.58 *	0.52 *	0.90 **	0.87 **	0.51 *	0.86 **	0.47	−0.65 **	0.95 **	0.91 **	1.00
Ni	−0.77 **	−0.68 **	−0.42	0.81 **	0.39	−0.30	−0.40	−0.74 **	−0.82 **	−0.28	−0.52 *	0.68 **	−0.65 *	−0.63 *	−0.59 *
Rb	0.83 **	0.94 **	0.24	−0.77 **	−0.59 *	0.51	0.91 **	0.85 **	0.48	0.86 **	0.47	−0.63 *	0.93 **	0.89 **	0.99 **
Ba	0.57 *	0.78 **	0.27	−0.60 *	−0.47	0.35	0.95 **	0.67 *	0.28	0.83 **	0.39	−0.44	0.81 **	0.83 **	0.86 **
Sr	−0.57 *	−0.60 *	−0.57 *	0.85 **	0.27	−0.40	−0.52	−0.60 *	−0.38	−0.40	−0.63 *	0.64 **	−0.58 *	−0.51 *	−0.54 *
Th	0.58 *	0.52 *	−0.07	−0.31	−0.49	0.15	0.17	0.55 *	0.71 **	0.39	0.14	−0.39	0.52 *	0.56 *	0.43
U	0.84 **	0.92 **	0.46	−0.75 **	−0.51	0.51	0.80 **	0.85 **	0.50 *	0.81 **	0.62 *	−0.65 **	0.94 **	0.91 **	0.90 **
Cu	−0.70 **	−0.77 **	−0.54 *	0.93 **	0.35	−0.50	−0.75 **	−0.74 **	−0.41	−0.57 *	−0.62 *	0.75 **	−0.74 **	−0.71 **	−0.75 **
Y	0.57 *	0.41	−0.15	−0.24	−0.63 *	−0.08	0.07	0.46	0.79 **	0.26	0.12	−0.32	0.39	0.44	0.36
Zr	0.86 **	0.69 **	0.46	−0.68 **	−0.40	0.24	0.29	0.72 **	0.90 **	0.34	0.57 *	−0.64 *	0.67 **	0.68 **	0.57 *
Pb	−0.71 **	−0.74 **	−0.47	0.91 **	0.31	−0.64 *	−0.51 *	−0.76 **	−0.37	−0.49	−0.53 *	0.84 **	−0.70 **	−0.64 *	−0.63 *
Zn	0.38	0.28	0.88 **	−0.27	0.11	0.04	0.15	0.19	0.24	0.15	0.76 **	−0.16	0.32	0.33	0.19
Nb	0.86 **	0.96 **	0.37	−0.80 **	−0.70 **	0.63 *	0.72 **	0.94 **	0.54 *	0.86 **	0.60 *	−0.66 **	0.95 **	0.91 **	0.88 **
Hf	0.38	0.41	0.83 **	−0.55 *	−0.16	0.41	0.36	0.44	0.23	0.29	0.71 **	−0.28	0.41	0.38	0.31
REE	0.77 **	0.55 *	0.28	−0.46	−0.45	0.00	0.21	0.57 *	0.95 **	0.25	0.46	−0.39	0.54 *	0.54 *	0.50

Table 4. *Cont.*

	Ni	Rb	Ba	Sr	Th	U	Cu	Y	Zr	Pb	Zn	Nb	Hf	REE
Si														
Al														
Fe														
Ca														
Mg														
Na														
K														
Ti														
P														
V														
Cr														
Co														
Ga														
Ta														
Cs														
Ni	1.00													
Rb	−0.57 *	1.00												
Ba	−0.40	0.87 **	1.00											
Sr	0.66 **	−0.54 *	−0.49	1.00										
Th	−0.41	0.38	0.31	−0.28	1.00									
U	−0.62 *	0.88 **	0.77 **	−0.44	0.32	1.00								
Cu	0.78 **	−0.76 **	−0.67 **	0.81 **	−0.10	−0.74 **	1.00							
Y	−0.50	0.33	0.19	−0.13	0.85 **	0.28	−0.10	1.00						
Zr	−0.85 **	0.52 *	0.36	−0.57 *	0.70 **	0.61 *	−0.58 *	0.71 **	1.00					
Pb	0.72 **	−0.62 *	−0.38	0.68 **	−0.15	−0.71 **	0.83 **	−0.12	−0.58 *	1.00				
Zn	−0.25	0.16	0.21	−0.29	0.02	0.44	−0.33	−0.08	0.44	−0.26	1.00			
Nb	−0.61 *	0.88 **	0.71 **	−0.54 *	0.50	0.88 **	−0.69 **	0.42	0.64 *	−0.67 **	0.32	1.00		
Hf	−0.47	0.31	0.35	−0.57 *	−0.07	0.45	−0.64 **	−0.15	0.43	−0.43	0.73 **	0.48	1.00	
REE	−0.72 **	0.47	0.32	−0.45	0.77 **	0.44	−0.37	0.83 **	0.91 **	−0.27	0.30	0.52 *	0.26	1.00

4. Results

4.1. Petrographic Observations

Petrographic examination of thin sections from the studied limestone samples reveals predominantly calcite-rich carbonate fabrics characterized by fine- to medium-crystalline calcite. Locally, micritic to microcrystalline carbonate domains are preserved, indicating minor textural heterogeneity within the carbonate matrix (Figure 2a,b). Variations in crystal size and the occurrence of locally more crystalline carbonate domains suggest limited recrystallization of the original carbonate fabric, resulting in the development of microsparitic textures in some areas (Figure 2a,b,d). These recrystallized domains are spatially restricted and do not occur uniformly throughout the examined thin sections.

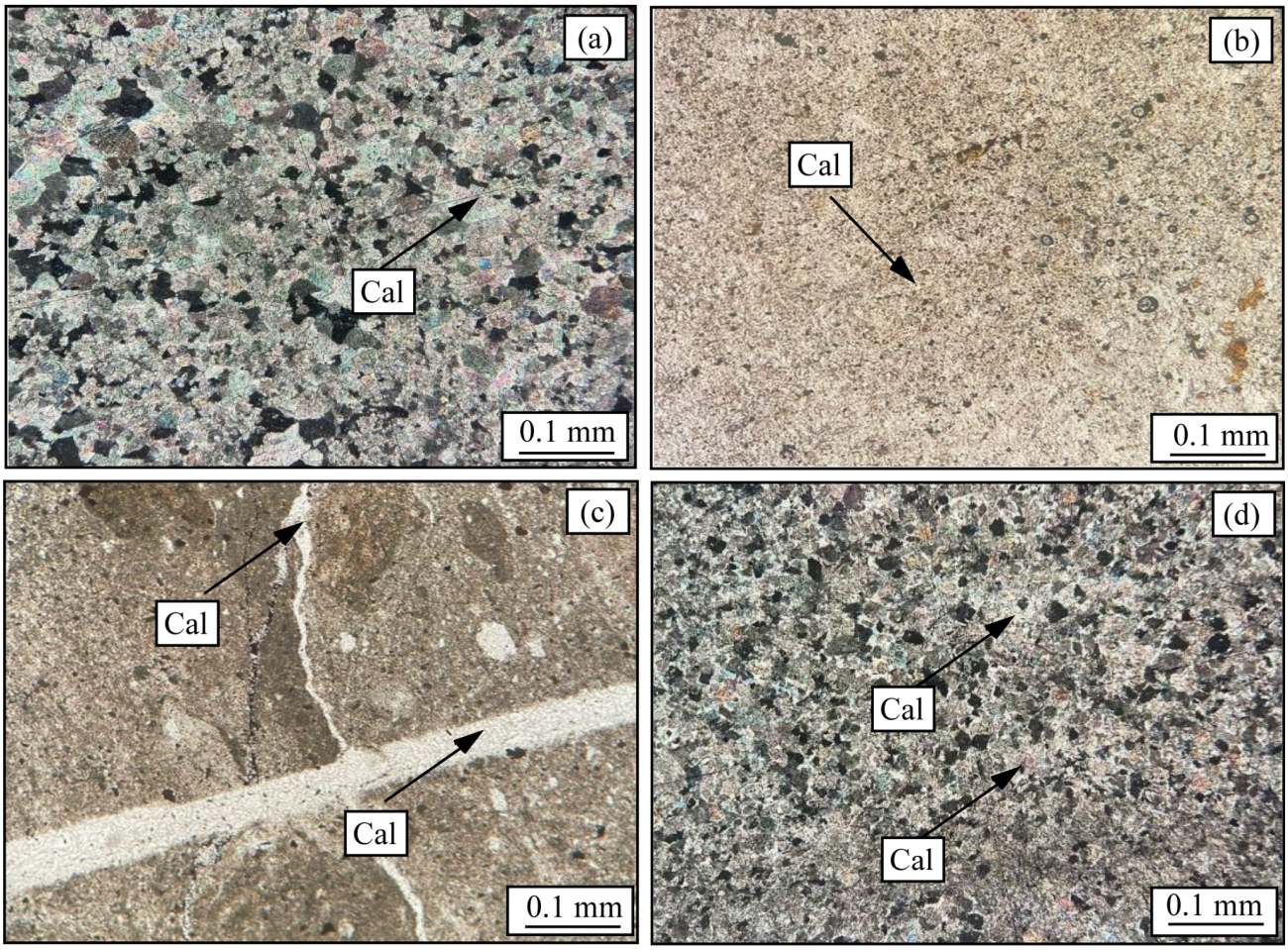


Figure 2. Representative photomicrographs illustrating the petrographic characteristics of the studied Tizkuh Formation limestones. (**a**,**b**) Calcite-dominated carbonate fabrics characterized by fine- to medium-crystalline calcite and locally preserved micritic to microcrystalline domains, with variations in crystal size. (**c**) A localized fracture- or vein-like feature filled with crystalline calcite, indicating minor post-depositional diagenetic modification. (**d**) Locally more crystalline calcite domains showing microsparitic textures. Calcite is indicated by Cal. Photomicrographs were taken under crossed-polarized light (XPL) for panels (**a**,**d**), and plane-polarized light (PPL) for panels (**b**,**c**).

Localized fracture- and vein-like features filled with crystalline calcite are observed in some samples, indicating minor post-depositional diagenetic modification of the limestone (Figure 2c). The development of these carbonate-filled fractures appears to be localized rather than pervasive within the studied samples. Minor non-carbonate constituents occur sporadically as dispersed grains and fine-grained aggregates within the carbonate matrix (Figure 2d). Although these phases are only locally observed petrographically, their

presence is consistent with the minor non-carbonate mineral components identified by X-ray diffraction analysis. Overall, the petrographic observations confirm the predominance of calcite-rich carbonate fabrics and indicate localized recrystallization and fracture-related diagenetic modification. The spatially restricted nature of these features suggests that post-depositional modification was heterogeneous within the studied samples rather than uniformly affecting the carbonate succession.

4.2. Mineralogy

The XRD results indicate a relatively consistent mineralogical composition among the studied limestones, with calcite consistently constituting the dominant mineral phase in all samples (Figure 3a,b; Table 1). The calcite-dominated assemblage is accompanied by variable proportions of non-carbonate and subordinate carbonate phases, including kaolinite, illite, quartz, dolomite, hematite, goethite, and plagioclase. Kaolinite and quartz occur consistently throughout the studied interval, whereas illite and dolomite are present in most samples. Hematite, goethite, and plagioclase occur only in a limited number of samples and generally represent minor to accessory phases.

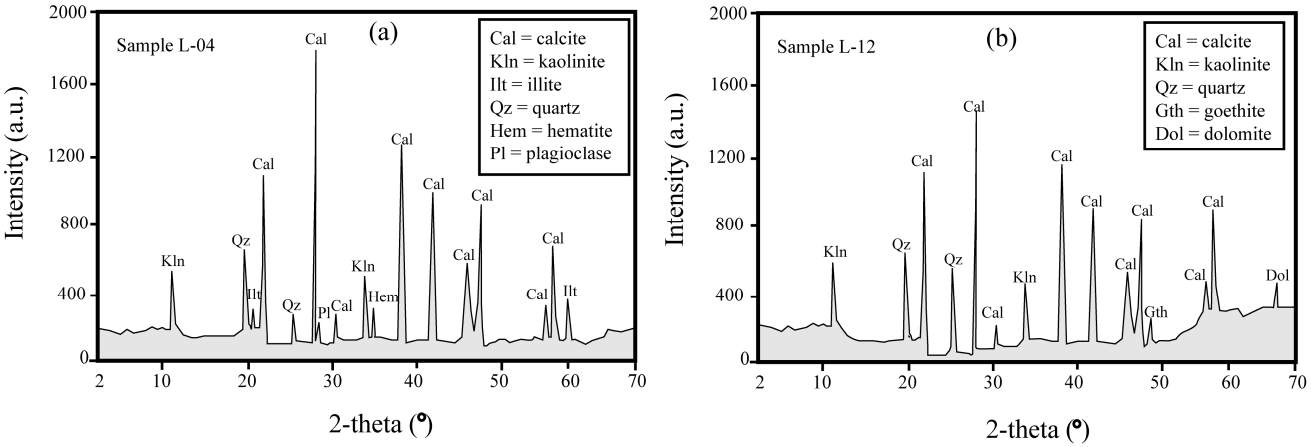


Figure 3. The XRD patterns of two selected samples, (**a**) L-04 and (**b**) L-12, from the studied limestones.

Quartz and plagioclase are interpreted as minor detrital siliciclastic components within the carbonate succession. The occurrence of plagioclase may also be compatible with input derived from nearby volcanic rocks, although the available mineralogical data do not permit identification of a specific source with certainty. The presence of these non-carbonate phases, particularly kaolinite and quartz, indicates that the carbonate samples contain variable amounts of aluminosilicate-bearing materials that may contribute to bulk-rock Al_2O_3 and associated trace-element abundances. Overall, the semi-quantitative XRD data indicate limited mineralogical variability along the studied stratigraphic interval, with calcite remaining the dominant phase throughout the profile. The XRD results are consistent with the petrographic observations, which show predominantly calcite-rich carbonate fabrics with minor dispersed non-carbonate components.

SEM–EDS examination of two selected samples provides additional microscale evidence for the mineralogical characteristics of the analyzed limestones (Figure 4). The SEM images show calcite as the dominant carbonate phase, together with locally occurring fine apatite crystals associated with the matrix calcite and, in places, present within intercrystalline spaces. The corresponding EDS spectra show characteristic elemental signatures of calcite, apatite, and kaolinite, supporting their qualitative identification (Figure 4). Since the SEM–EDS analyses were conducted on only two selected samples, these observations

are considered complementary evidence for the occurrence of these phases in the analyzed samples and are not generalized to the entire succession.

Nevertheless, the identification of apatite is relevant to the interpretation of the bulk-rock geochemical data because phosphate-bearing phases may contribute to the bulk-rock REE inventory. Similarly, the presence of kaolinite and other aluminosilicate-bearing phases provides a potential mineralogical basis for evaluating the influence of detrital materials on Al_2O_3 and REE abundances. The potential contributions of phosphate-bearing and aluminosilicate components to the bulk-rock REE inventory are therefore further evaluated using elemental correlations and Al_2O_3-normalized REE patterns.

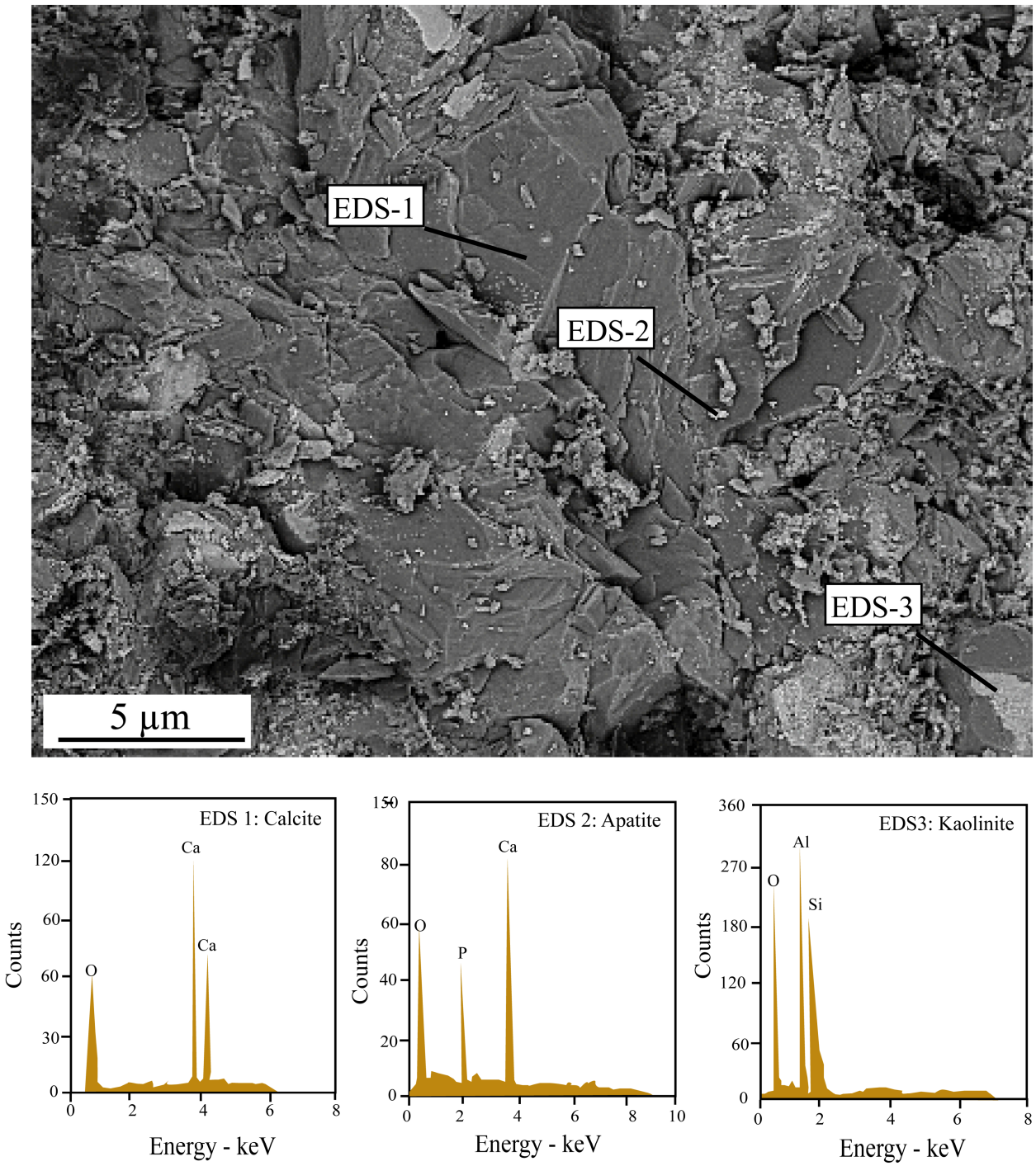


Figure 4. Representative SEM images and corresponding EDS spectra for the qualitative identification of calcite, kaolinite, and apatite in sample L-09 from the studied limestone samples.

4.3. Major- and Trace-Element Geochemistry

The major-element compositions show that CaO is the most abundant component in the studied limestones, ranging from 35.58 to 42.66 wt% (average: 39.79 ± 2.22 wt%; Table 2). MgO occurs in relatively low concentrations, ranging from 0.74 to 0.85 wt% (average: 0.80 ± 0.03 wt%). The concentrations of SiO_2, Al_2O_3, and Fe_2O_3 range from 12.62 to 16.35 wt%, 4.36 to 6.06 wt%, and 1.82 to 2.03 wt%, respectively. The other oxides, including Na_2O, K_2O, TiO_2, MnO, and P_2O_5, occur in low concentrations and collectively account for 0.88–1.29 wt% of the bulk-rock composition. The LOI values range from 35.24 to 40.19 wt%. The CaO/MgO ratios vary from 42.87 to 54.26 (Table 3). The relatively high CaO contents together with variable SiO_2 and Al_2O_3 concentrations indicate variations in the relative proportions of the carbonate and non-carbonate components among the studied samples.

The trace-element concentrations show relatively limited variations among the studied limestones (Table 2). V, Cr, Co, Ni, and Cu range from 18 to 26 ppm, 10 to 30 ppm, 2.9 to 4.9 ppm, 16 to 23 ppm, and 8 to 25 ppm, respectively. The lithophile elements Rb, Cs, Ga, Nb, Ta, and Hf occur at relatively low concentrations (≤13.6 ppm). Among the analyzed trace elements, Sr shows the highest concentrations, ranging from 147.6 to 261.2 ppm. Y, Zr, Th, and U range from 4.2 to 6.5 ppm, 21 to 41 ppm, 7.15 to 10.09 ppm, and 0.38 to 0.91 ppm, respectively. Ba, Pb, and Zn range from 13.5 to 17.3 ppm, 17 to 21 ppm, and 21 to 35 ppm, respectively. The U/Th ratios range from 0.04 to 0.11, with an average of 0.07 ± 0.02 (Table 3).

Correlation analysis shows systematic relationships among several major and trace elements (Table 4). CaO exhibits negative correlations with SiO_2 (Figure 5a), Al_2O_3 (Figure 5b), K_2O, TiO_2, V, Cr, Ga, Ta, Cs, Rb, Ba, U, Zr, and Nb, with correlation coefficients ranging from −0.59 to −0.87. The inverse relationships between CaO and Al_2O_3 and SiO_2 indicate that variations in carbonate abundance are accompanied by corresponding changes in the non-carbonate fraction, consistent with variable mixing between a calcite-dominated component and an aluminosilicate-rich component. In contrast, SiO_2 and Al_2O_3 show positive correlations with TiO_2, Ga (Figure 5c), Nb (Figure 5d), and Ta (Figure 5e) (r = 0.83–0.99). These associations indicate that Al_2O_3 and SiO_2 covary with elements commonly associated with the non-carbonate siliciclastic fraction, providing geochemical support for variable terrigenous input. Positive relationships are also observed between SiO_2 and Zr (r = 0.86) (Figure 5f), K_2O and Rb (r = 0.91) (Figure 5g), and K_2O and Cs (r = 0.90) (Figure 5h). Fe_2O_3 exhibits positive correlations with Zn (r = 0.88) (Figure 5i), Cr (r = 0.83) (Figure 5j), and Hf (r = 0.88) (Figure 5k). U shows positive correlations with Al_2O_3 (r = 0.92) (Figure 5l), SiO_2 (r = 0.84), TiO_2 (r = 0.85), Rb (r = 0.88), Cs (r = 0.90), and Nb (r = 0.88), whereas CaO is positively correlated with Sr (r = 0.85) (Figure 5m), Pb (r = 0.91) (Figure 5n), Cu (r = 0.93) (Figure 5o), and Co (r = 0.85) (Figure 5p). Taken together, these relationships indicate that a substantial part of the whole-rock geochemical variability is related to changes in the relative proportions of carbonate and non-carbonate material. This compositional control is important when evaluating bulk-rock REE abundances because variations in the proportion of the carbonate fraction may dilute or concentrate elements associated with the non-carbonate component.

4.4. REE Characteristics

The total rare earth element concentrations (ΣREE) range from 31.54 to 62.18 ppm, with an average of 42.35 ± 9.40 ppm (Table 3). The ΣLREE and ΣHREE concentrations range from 28.82 to 57.75 ppm (average: 38.99 ± 8.86 ppm) and 2.72 to 4.43 ppm (average: 3.37 ± 0.57 ppm), respectively. Among the REE, Ce is the most abundant element, with

concentrations ranging from 11.9 to 26.8 ppm, followed by La (7.6–14.9 ppm) and Nd (6.2–10.8 ppm).

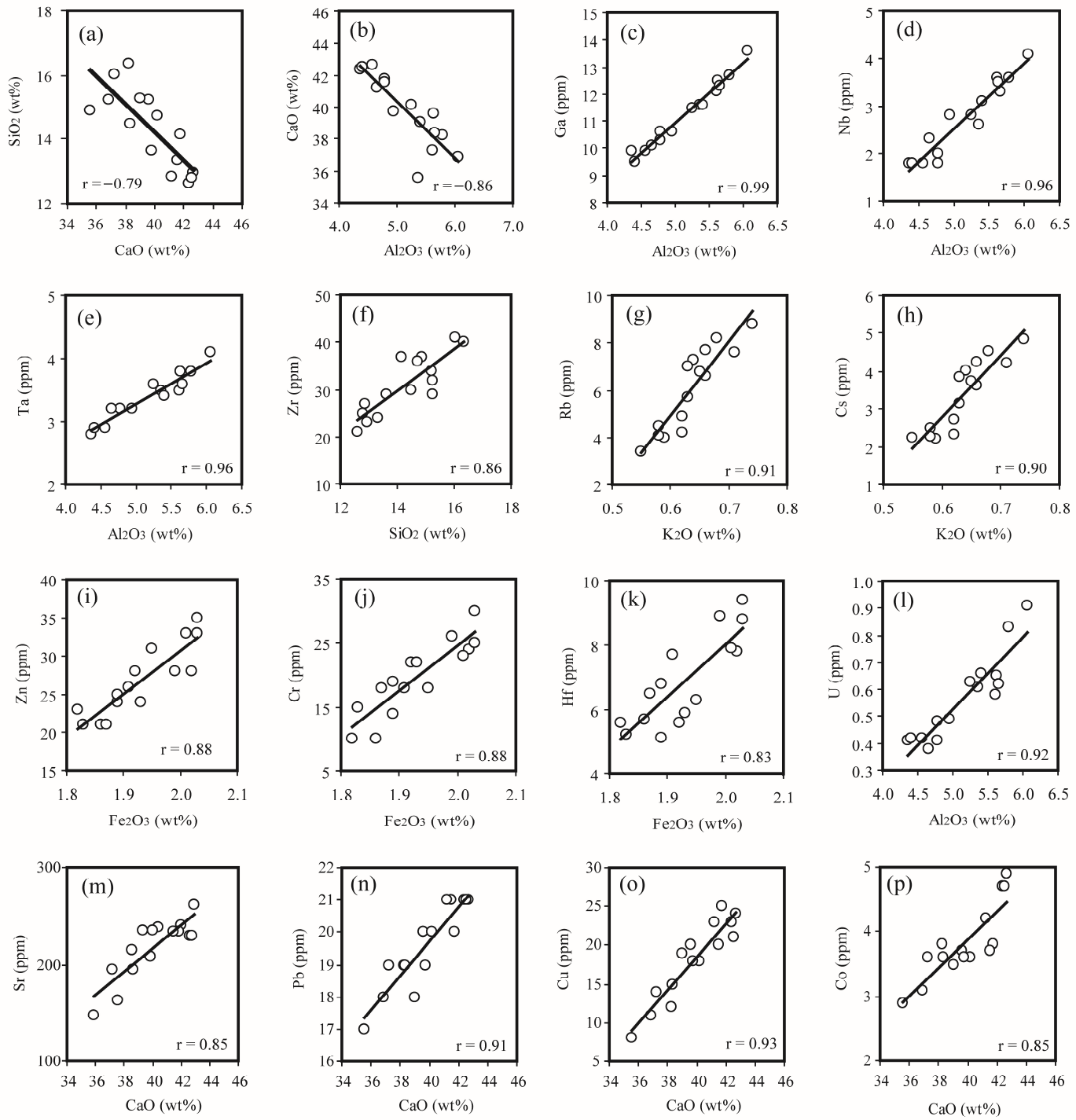


Figure 5. Bivariate diagrams of (**a**) SiO_2–CaO, (**b**) Al_2O_3–CaO, (**c**) Al_2O_3–Ga, (**d**) Al_2O_3–Nb, (**e**) Al_2O_3–Ta, (**f**) SiO_2–Zr, (**g**) K_2O–Rb, (**h**) K_2O–Cs, (**i**) Fe_2O_3–Zn, (**j**) Fe_2O_3–Cr, (**k**) Fe_2O_3–Hf, (**l**) Al_2O_3–U, (**m**) CaO–Sr, (**n**) CaO–Pb, (**o**) CaO–Cu, and (**p**) CaO–Co plotted for the studied limestones of the Tizkuh Formation.

The ΣREE values show a negative correlation with CaO (r = −0.46) (Figure 6a) and positive correlations with SiO_2 (r = 0.77) (Figure 6b), Al_2O_3 (r = 0.90), Th (r = 0.76) (Figure 6c), Y (r = 0.83) (Figure 6d), Zr (r = 0.91) (Figure 6e), and P_2O_5 (r = 0.95) (Figure 6f). The strong positive relationship between ΣREE and Al_2O_3, together with the positive associations of

ΣREE with SiO_2, Th, and Zr, indicates that variations in the bulk-rock REE inventory are closely associated with the non-carbonate fraction. The positive relationship with P_2O_5 further indicates a contribution from phosphate-bearing phases. The Y/Ho ratios range from 23.89 to 30.38, with an average of 26.84 ± 2.31.

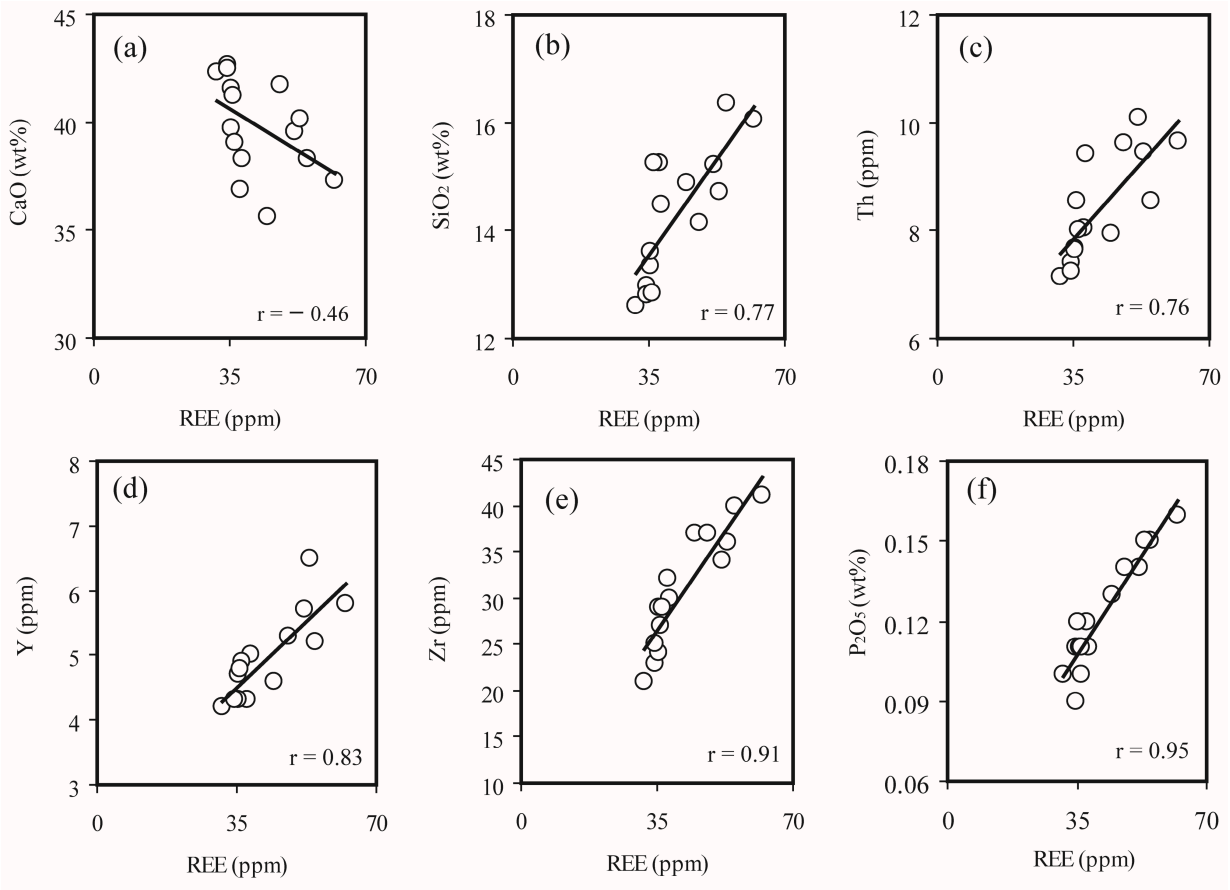


Figure 6. Bivariate diagrams of REE versus (**a**) CaO, (**b**) SiO_2, (**c**) Th, (**d**) Y, (**e**) Zr, and (**f**) P_2O_5 drawn for the studied limestones of the Tizkuh Formation.

To further evaluate whether the observed variations in absolute REE concentrations are primarily related to differences in the relative proportions of the carbonate and non-carbonate materials, the REE concentrations were additionally normalized to Al_2O_3. The resulting REE/Al_2O_3 patterns for the 15 samples show broadly similar, systematic zigzag-like distributions (Figure 7). Despite differences in absolute REE abundances, the overall relative shapes of the Al_2O_3-normalized patterns are broadly consistent among the samples. This similarity indicates that variations in the absolute concentrations of REEs are partly related to differences in the relative abundance of the non-carbonate component, whereas the overall REE fractionation pattern is not solely controlled by variations in carbonate dilution. The normalized REE patterns and the relevant REE ratios are presented in Figure 8 and Table 3.

The values of $(La/Yb)_N$ and $(Nd/Yb)_N$ range from 1.35 to 1.89 (average: 1.63 ± 0.13) and 1.19 to 1.67 (average: 1.46 ± 0.16), respectively. The Er/Nd ratios range from 0.06 to 0.08. These values indicate relatively limited LREE–HREE fractionation among the studied samples. This feature is also evident in the PAAS-normalized REE distribution pattern (Figure 8).

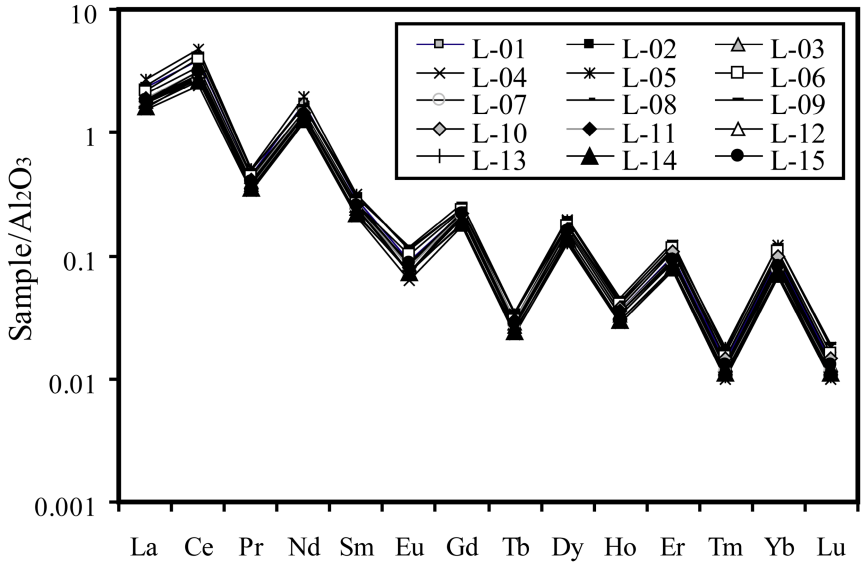


Figure 7. Al_2O_3-normalized REE patterns of the Tizkuh Formation limestones. REE concentrations were normalized to Al_2O_3 to evaluate REE distributions relative to the terrigenous/aluminosilicate component and to assess whether the observed REE patterns are consistent among the samples with variable proportions of non-carbonate materials.

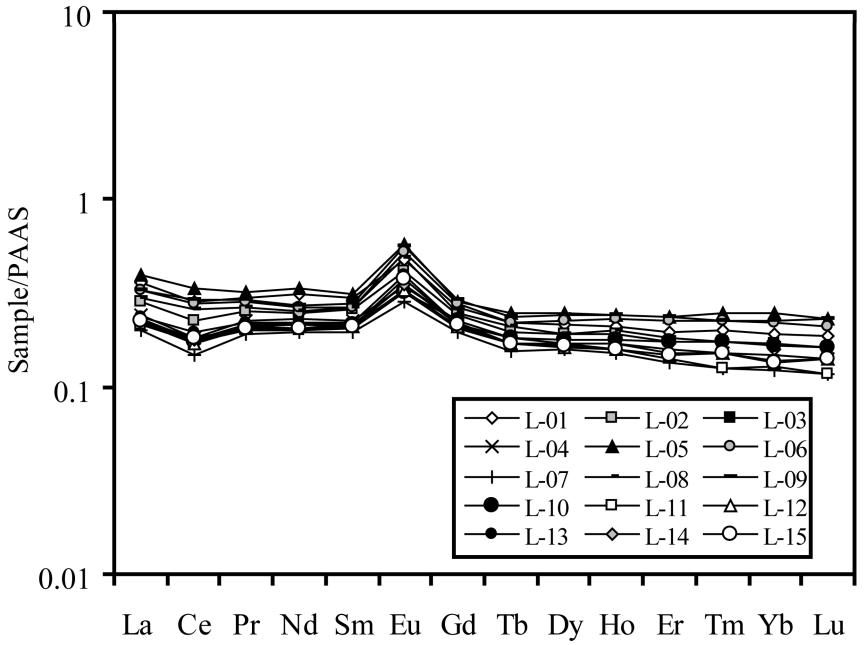


Figure 8. Plot of the PAAS-normalized REE distribution patterns [28] for the studied limestones of the Tizkuh Formation.

4.5. Ce and Eu Anomalies

The Ce/Ce* values of the studied limestones range from 0.76 to 0.94, with an average of 0.85 ± 0.06. The corresponding Pr/Pr* values range from 0.96 to 1.13. The Ce/Ce* versus Pr/Pr* relationship and the relationships between Ce/Ce* and selected major and trace elements are shown in Figures 9 and 10.

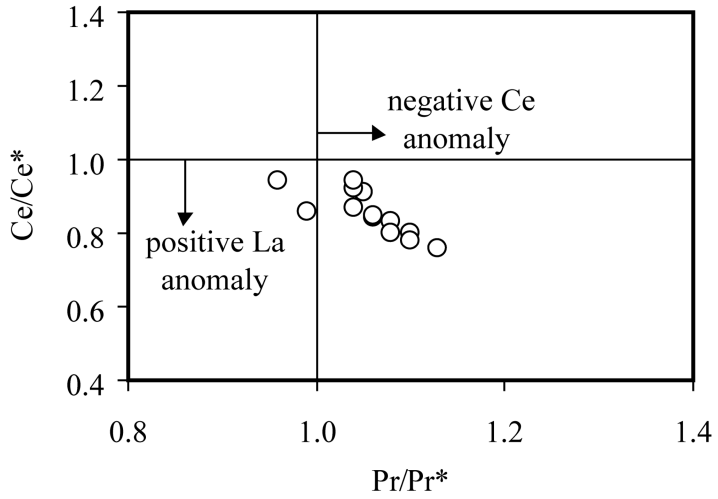


Figure 9. Bivariate plot of Ce/Ce* versus Pr/Pr* (normalized to PAAS) for the assessment of La and Ce anomalies using the method of Bau and Dulski [3] (modified after [14]) for the studied limestones of the Tizkuh Formation.

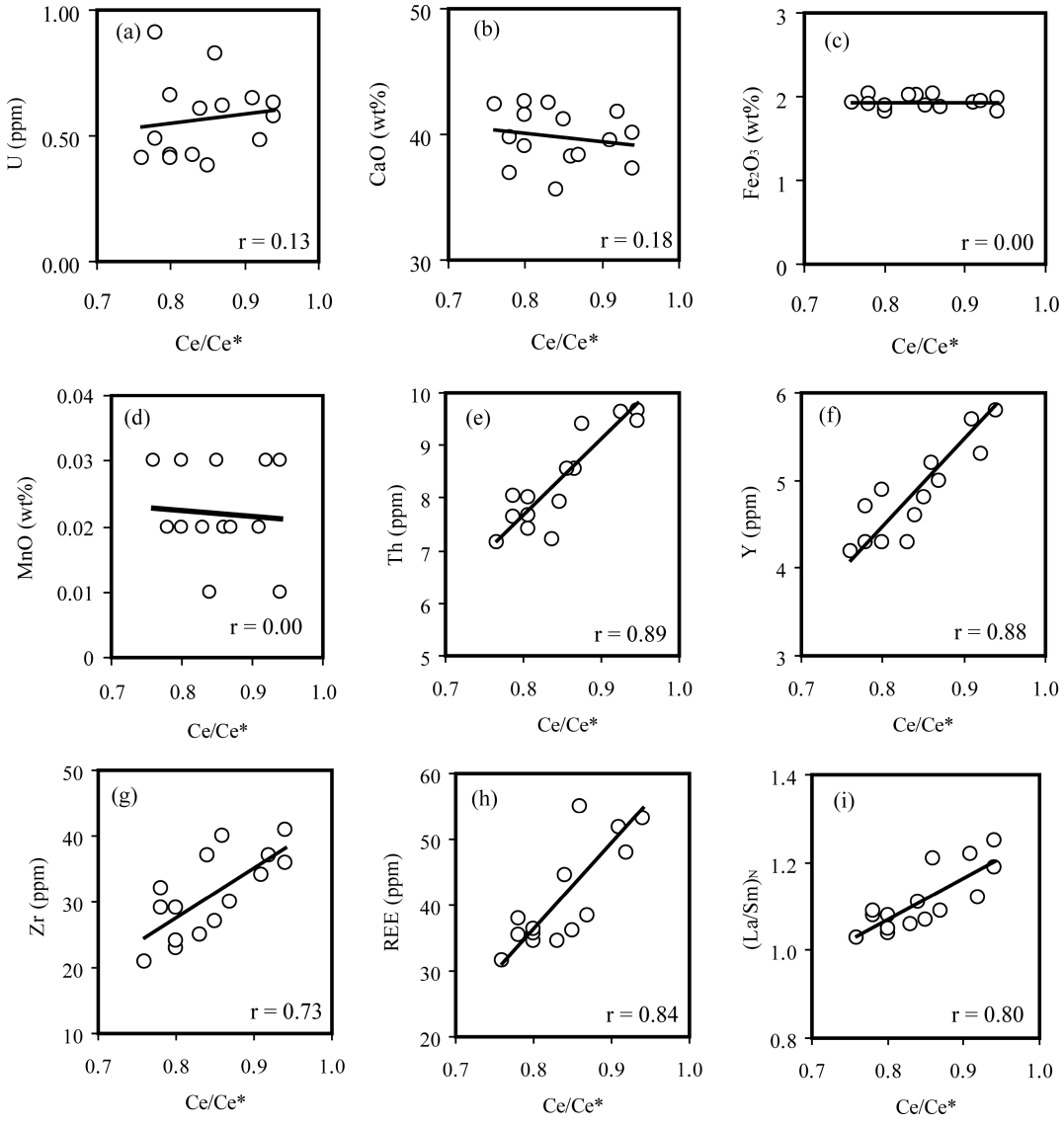


Figure 10. Bivariate diagrams of Ce/Ce* versus (**a**) U, (**b**) CaO, (**c**) Fe_2O_3, (**d**) MnO, (**e**) Th, (**f**) Y, (**g**) Zr, (**h**) REE, and, (**i**) $(La/Sm)_N$, drawn for the studied limestones of the Tizkuh Formation.

The Ce/Ce* values show no significant correlations with U (r = 0.13) (Figure 10a), CaO (r = 0.18) (Figure 10b), Fe_2O_3 (r = 0.00) (Figure 10c), and MnO (Figure 10d). In contrast, Ce/Ce* shows positive correlations with Th (r = 0.89) (Figure 10e), Y (r = 0.88) (Figure 10f), Zr (r = 0.73) (Figure 10g), and ΣREE (r = 0.84) (Figure 10h). A positive correlation is also observed between Ce/Ce* and $(La/Sm)_N$ (r = 0.80) (Figure 10i).

The Eu/Eu* values vary from 1.44 to 1.98 with an average of 1.70 ± 0.18. The Eu/Eu* exhibits negative relationships with the ratios of Ba/Nd (r = −0.63) (Figure 11a) and Ba/Sm (r = −0.65) (Figure 11b), whereas its relationship with Ba is not significant (r = 0.15) (Figure 11c). Positive correlations are observed between Eu/Eu* and ΣREE (r = 0.75) (Figure 11d), Ce/Ce* (r = 0.93) (Figure 11e), Th (r = 0.91) (Figure 11f), Y (r = 0.89) (Figure 11g), and Zr (r = 0.67) (Figure 11h). The relationship between Eu/Eu* and Na_2O/Al_2O_3 is shown in Figure 11i.

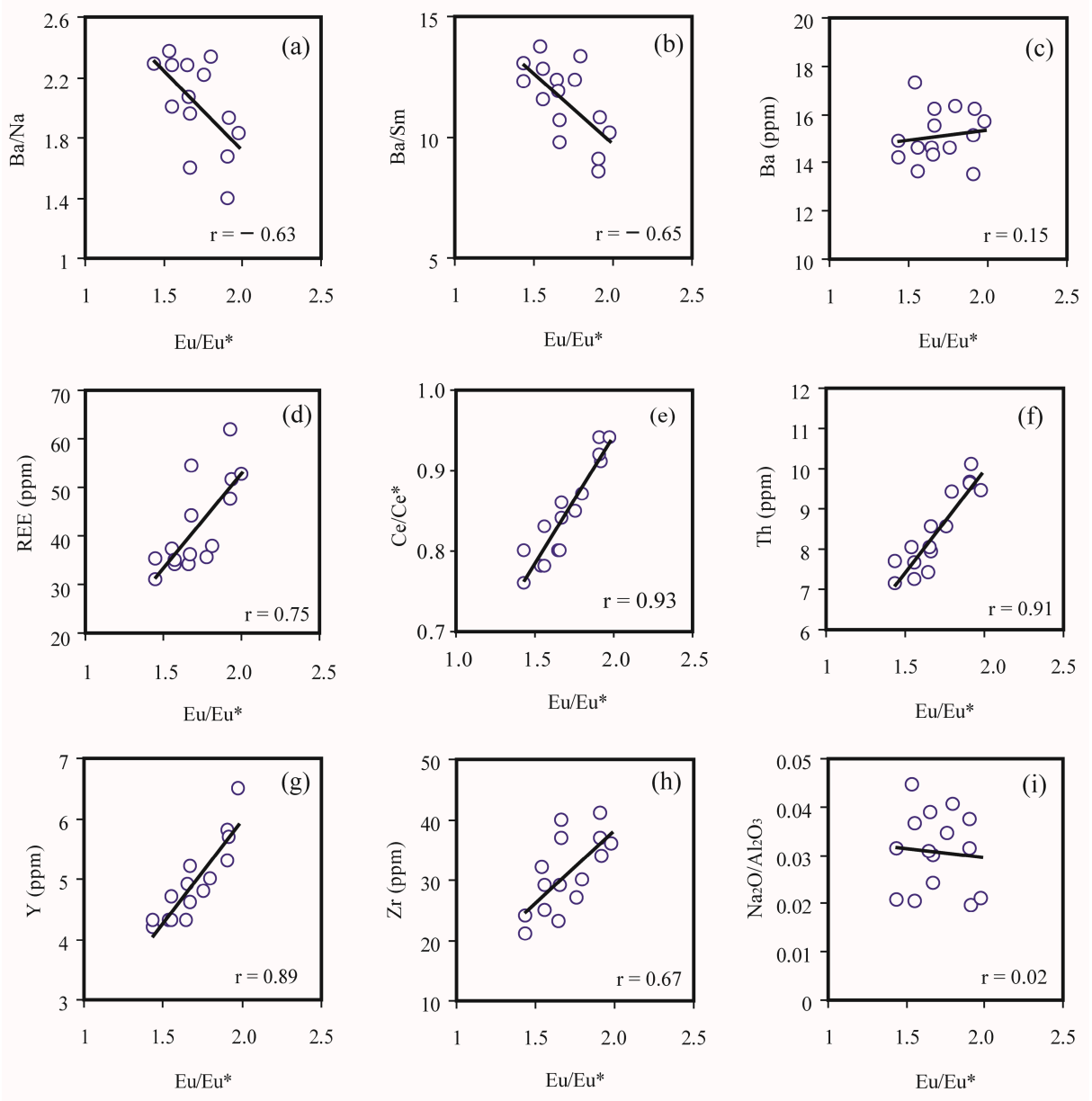


Figure 11. Bivariate diagrams of Eu/Eu* versus (**a**) Ba/Nd, (**b**) Ba/Sm, (**c**) Ba, (**d**) REE, (**e**) Ce/Ce*, (**f**) Th, (**g**) Y, (**h**) Zr, and (**i**) Na_2O/Al_2O_3 for the studied limestones of the Tizkuh Formation.

5. Discussion

5.1. Controls on the Distribution of Major and Trace Elements in the Tizkuh Limestones

The correlation coefficients (Table 4), together with the mineralogical results (Table 1), provide constraints on the processes controlling the distribution of major and trace elements in the limestones of the Tizkuh Formation. Because the correlation analysis is based on a relatively small dataset (n = 15), individual Pearson correlation coefficients were interpreted cautiously and in conjunction with mineralogical and other geochemical evidence. Statistical significance was assessed using two-tailed tests and is indicated in Table 4 by one and two asterisks for $p < 0.05$ and $p < 0.01$, respectively. In addition, potential compositional closure effects were considered, particularly when interpreting correlations among major-element concentrations. Therefore, the reported correlations are regarded as indicators of geochemical association rather than definitive evidence of direct mineralogical or process-specific controls.

The negative correlations of CaO with SiO_2 (r = −0.79) (Figure 5a), Al_2O_3 (r = −0.86) (Figure 5b), K_2O (r = −0.67), TiO_2 (r = −0.87), V (r = −0.62), Cr (r = −0.59), Ga (r = −0.85), Ta (r = −0.78), Cs (r = −0.77), Rb (r = −0.77), Ba (r = −0.60), U (r = −0.75), Zr (r = −0.68), and Nb (r = −0.80) indicate an inverse relationship between the carbonate component and several non-carbonate-associated elements. This pattern is consistent with a carbonate dilution effect, whereby increasing carbonate accumulation reduces the apparent concentrations of elements predominantly associated with the non-carbonate fraction [48]. Accordingly, variations in the relative proportions of carbonate and siliciclastic materials represent an important control on whole-rock geochemical variability in the studied limestones [49]. The relatively elevated SiO_2 concentrations (12.62–16.35 wt%) are therefore interpreted to primarily reflect variable input of fine-grained terrigenous/siliciclastic materials, consistent with the presence of quartz and clay-bearing aluminosilicate phases and the negative correlation between SiO_2 and CaO (r = −0.79).

The quartz and plagioclase identified in the studied limestones are interpreted primarily as minor detrital components introduced through limited siliciclastic input to the carbonate platform. Quartz most likely represents a mechanically transported mineral derived from quartz-bearing continental source rocks, whereas the minor plagioclase may have originated from feldspar-bearing continental or volcanic rocks. The occurrence of quartz and kaolinite, together with the positive associations among SiO_2, Al_2O_3, TiO_2, Zr, Nb, Ta, and Ga and the negative relationships between CaO and several detrital-related elements, supports a predominantly terrigenous contribution to the non-carbonate fraction. However, the available bulk-rock mineralogical and geochemical data do not permit discrimination among specific source lithologies with confidence.

The strong positive correlations of SiO_2 and Al_2O_3 with TiO_2, Ga (Figure 5c), Nb (Figure 5d), and Ta (Figure 5e) (r = 0.83–0.99), together with the positive relationships between SiO_2–Zr (r = 0.86) (Figure 5f), K_2O–Rb (r = 0.91) (Figure 5g), and K_2O–Cs (r = 0.90) (Figure 5h), indicate consistent geochemical associations among these elements. Ti, Zr, Nb, Ta, and Ga are generally characterized by low mobility during weathering and sedimentary transport and are therefore commonly used as indicators of detrital input and provenance [50]. The strong relationships among these elements suggest that they were largely associated with the siliciclastic components of the limestones. Although kaolinite and illite were identified mineralogically, the bulk-rock correlation data do not allow these elements to be assigned uniquely to a particular clay mineral [50,51].

The distribution of several transition and trace elements is also associated with Fe-bearing phases and/or the non-carbonate fraction. The positive correlations of Fe_2O_3 with Zn (r = 0.88) (Figure 5i), Cr (r = 0.83) (Figure 5j), and Hf (r = 0.88) (Figure 5k) may reflect a common detrital contribution and/or association with Fe-bearing phases such as hematite

and goethite [52,53]. However, the whole-rock data alone are insufficient to demonstrate specific adsorption onto Fe-oxyhydroxides. The transition elements V, Cr, Co, Ni, and Cu occur at relatively low to moderate concentrations in the studied limestones. Their variable concentrations likely reflect differences in the relative proportions of the carbonate and non-carbonate components, together with the availability of different trace-element-bearing phases. The positive relationship between Cr and Fe_2O_3 suggests that Fe-bearing phases may have contributed to Cr retention, whereas the positive relationships between CaO and Cu and Co indicate that part of their variability may be associated with the carbonate component. The distribution of V, Cr, Co, Ni, and Cu may therefore reflect multiple processes, including detrital input, association with Fe-bearing phases, partial incorporation or retention within carbonate-associated phases, and limited post-depositional redistribution. Given the available mineralogical and bulk-rock data, no single mineralogical carrier can be identified as the dominant source for all of these transition elements, and the relative contribution of the individual mechanisms cannot be quantitatively distinguished.

The relatively elevated Th concentrations (7.15–10.09 ppm) are unlikely to be associated predominantly with the carbonate phase because Th is strongly particle-reactive and is commonly concentrated in detrital aluminosilicate and accessory minerals. The positive relationships of Th with SiO_2, Zr, Y, and ΣREE therefore suggest that its occurrence in the studied limestones is mainly related to the non-carbonate fraction, particularly fine-grained siliciclastic material and associated accessory phases. Similarly, the strong positive correlations of U with Al_2O_3 (r = 0.92) (Figure 5l), SiO_2 (r = 0.84), TiO_2 (r = 0.85), Rb (r = 0.88), Cs (r = 0.90), and Nb (r = 0.88), together with its negative correlation with CaO (r = −0.75), suggest an important contribution from the fine-grained detrital component. A portion of U may also have been associated with clay-rich material through surface adsorption. However, the present bulk-rock dataset does not allow the relative contribution of individual Th- and U-bearing minerals to be quantitatively determined. The observed U variability is therefore more plausibly related to changes in the proportion of non-carbonate material than to redox variations alone [6,9]. The absence of a significant correlation between Ce/Ce* and U (r = 0.13) (Figure 10a) does not provide strong evidence for a direct relationship between Ce-anomaly variability and U concentrations. Because U can be mobile during post-depositional alteration, U alone is not considered a sufficiently robust independent proxy for evaluating the preservation of primary redox signals in carbonate rocks. Therefore, the U data were evaluated together with the U/Th ratio and other mineralogical and geochemical indicators. The U/Th ratios range from 0.04 to 0.11, with an average of 0.07 ± 0.02 (Table 3), and are considered consistent with predominantly oxic conditions. However, given the potential mobility of U during diagenesis and the limited sample size, the U/Th ratio is used only as supporting evidence rather than as a definitive redox proxy.

The strong positive correlations of CaO with Sr (r = 0.85) (Figure 5m), Pb (r = 0.91) (Figure 5n), Cu (r = 0.93) (Figure 5o), and Co (r = 0.85) (Figure 5p) suggest associations between these elements and the carbonate component. The strong CaO–Sr relationship is consistent with the well-known incorporation of Sr into the calcite crystal lattice, whereas the relationships of Pb, Cu, and Co with CaO may reflect their occurrence in or interaction with carbonate phases. Nevertheless, whole-rock correlations do not demonstrate direct incorporation of Pb, Cu, or Co into calcite. Sr can readily substitute for Ca in calcite because of its similar ionic characteristics, whereas Co, Pb, and Cu may undergo redistribution during recrystallization and limited water–rock interaction [54].

It should also be emphasized that the correlation coefficients were calculated from whole-rock compositional data. Consequently, some relationships may be affected by compositional closure, whereby changes in the relative abundance of major components

can generate correlations among constituents even when their absolute concentrations are not directly coupled. Accordingly, the observed correlations are interpreted as evidence of geochemical associations rather than definitive proof of specific mineral hosts or processes.

The Mn/Sr ratio was used as one of several indicators of diagenetic modification. The values range from 0.48 to 1.01, with an average of 0.77 ± 0.18. Because Sr may be progressively released from the calcite crystal lattice during recrystallization, whereas Mn can be incorporated into diagenetic calcite, increasing Mn/Sr ratios have commonly been used as an indicator of increasing diagenetic modification [54–58]. The Mn/Sr values below 2 are consistent with relatively limited to moderate diagenetic modification [55]. However, recent studies emphasize that the Mn/Sr value alone is insufficient to assess the extent of diagenetic alteration or the preservation of primary geochemical signatures, and it should therefore be evaluated together with independent mineralogical and geochemical evidence [54,58,59]. Accordingly, Mn/Sr is considered here only as one indicator of diagenetic modification and is not used as independent evidence for the preservation of primary Ce anomalies [54,58,59].

The relatively restricted range of Mn/Sr values suggests broadly comparable degrees of diagenetic modification among the sampled limestones. Nevertheless, this ratio does not demonstrate that the primary geochemical composition was fully preserved. Assessment of preservation should instead consider multiple independent indicators, including Y/Ho ratios, normalized REE patterns, Ce and Eu anomalies, detrital contamination, U/Th, and mineralogical evidence [16,23,54,58,60].

The CaO/MgO ratios provide complementary information on carbonate mineralogy. The values of this ratio in the studied samples range from 42.87 to 54.26, indicating a predominance of calcite and a limited contribution of dolomite or other Mg-bearing phases [61,62]. These data do not support pervasive dolomitization of the studied limestones. However, CaO/MgO should not be regarded as an independent measure of limestone purity because the bulk composition is also affected by siliciclastic and other minor phases.

The relationship between carbonate dilution and REE variability provides an additional constraint on the interpretation of the REE data. The positive correlation between ΣREE and Al_2O_3 (r = 0.55), together with the positive relationships of ΣREE with SiO_2 (Figure 6b), Th (Figure 6c), Zr (Figure 6e), and P_2O_5 (Figure 6f), indicates that a substantial part of the bulk-rock REE inventory is associated with the non-carbonate fraction, including siliciclastic and phosphate-bearing components. Accordingly, differences in absolute ΣREE concentrations should not be interpreted directly as changes in the concentration of REEs in the depositional seawater. Rather, they partly reflect differences in the relative proportions of the carbonate and REE-bearing non-carbonate materials.

This interpretation is further supported by the Al_2O_3-normalized REE patterns (Figure 7). Despite the differences in absolute ΣREE concentrations among the samples, the 15 samples display broadly similar REE/Al_2O_3 patterns and comparable relative distributions among individual REE. The persistence of similar normalized patterns indicates that carbonate dilution contributes substantially to variations in absolute REE abundances, but does not by itself account for the overall REE fractionation pattern. Thus, the REE characteristics of the Tizkuh limestones reflect both variable mixing between the carbonate and non-carbonate components and additional mineralogical and post-depositional controls.

Overall, the distribution of major and trace elements in the studied limestones appears to have been controlled principally by three interacting processes: (1) carbonate production and accumulation, together with dilution of the non-carbonate elements; (2) variable but generally limited input of siliciclastic material, which was particularly important for the immobile and lithophile elements; and (3) limited to moderate diagenetic modification,

which resulted in restricted redistribution of some mobile elements. The additional relationship between ΣREE and Al_2O_3 and the broadly consistent Al-normalized REE patterns demonstrate that the carbonate–non-carbonate mixing and associated dilution are also important considerations when interpreting the absolute REE concentrations. These processes partially modified the original geochemical composition but did not necessarily eliminate all depositional information. This framework provides the basis for evaluating the REE characteristics and the extent to which selected marine and redox-related features may have been retained.

5.2. Controls on REE Distribution and Fractionation in the Tizkuh Carbonate Platform

The ΣREE concentrations in the studied limestones range from 31.54 to 62.18 ppm, with an average of 42.35 ± 9.40 ppm (Table 3). These values fall within the range reported for many Phanerozoic, particularly Mesozoic, marine carbonate rocks and do not indicate anomalous bulk-rock REE enrichment [14,16,23,26,54]. The average ΣREE concentration is lower than that reported for Arabian Sea marine sediments (78 ± 40 ppm) [63] but is comparable to or slightly higher than values reported for some shallow-marine limestones (32.2 ± 13.3 ppm) [64] (Table 5).

The negative correlation between ΣREE and CaO (r = −0.46) (Figure 6a) indicates that carbonate dilution contributed to variations in bulk-rock REE concentrations. As carbonate accumulation increases, the apparent concentration of REE per unit mass of rock may decrease because calcite generally contains substantially lower REE concentrations than silicate and phosphate phases [14,16,23,26,54,58]. This relationship therefore suggests that variations in carbonate versus non-carbonate proportions represent an important control on the bulk-rock REE concentrations. However, the ΣREE–CaO relationship alone provides only moderate evidence for this effect. More direct support is provided by the positive correlation between ΣREE and Al_2O_3 (r = 0.55), because Al_2O_3 is closely associated with the variable non-carbonate fraction in the studied limestones. Together with the negative correlations between CaO and Al_2O_3 (r = −0.86) and between CaO and several detrital-related elements, this relationship indicates that differences in the relative proportions of the carbonate and non-carbonate material exert a substantial control on absolute bulk-rock REE concentrations.

The role of terrigenous material is indicated by the positive correlations of ΣREE with SiO_2 (r = 0.77), Th (r = 0.76), Y (r = 0.83), and Zr (r = 0.91). Clay minerals and other fine-grained detrital particles can contribute to the bulk-rock REE inventory because of their large specific surface area and capacity to retain trace elements [23,65,66]. The relationship between ΣREE and Th is particularly consistent with a contribution from the lithogenic fraction because Th is relatively immobile during weathering and sedimentary transport [47,66,67]. Such integrated use of mineralogical and elemental geochemical relationships is also consistent with recent provenance and paleoenvironmental studies that emphasize the importance of distinguishing detrital contributions from depositional signals when reconstructing sedimentary environments [67]. These relationships indicate that the bulk-rock REE inventory was substantially influenced by the non-carbonate component and therefore cannot be regarded as a direct representation of contemporaneous seawater composition.

The Al_2O_3-normalized REE patterns provide an additional test for the dilution effect. Despite the differences in absolute ΣREE concentrations among the 15 samples, the Al_2O_3-normalized patterns display broadly similar and systematic distributions among the individual REE (Figure 7). This consistency indicates that variations in absolute REE abundances are partly related to changes in the relative abundance of the non-carbonate component, whereas the overall relative REE distribution and fractionation pattern are not

solely produced by carbonate dilution. Thus, carbonate dilution is considered an important control on REE concentration, but it does not fully explain the observed REE fractionation.

Phosphate phases represent another potentially important control on the REE budget. The very strong positive correlation between ΣREE and P_2O_5 (r = 0.95) (Figure 6f), together with the identification of fine apatite crystals by SEM–EDS in two selected samples, suggests that phosphates acted as host mineral phases and contributed substantially to REE concentration in at least a part of the studied succession [68,69]. However, because SEM–EDS observations were limited to two selected samples, the abundance and relative importance of apatite cannot be generalized to the entire succession. The ΣREE–P_2O_5 relationship therefore provides strong evidence for a phosphate-related control on the bulk-rock REE inventory, but it does not permit quantitative determination of the amount of REE hosted by apatite.

Apatite may accommodate REE through substitution for Ca and can potentially exchange REE with intergranular fluids during early diagenesis [70,71]. Thus, phosphate phases may have contributed to both REE accumulation and subsequent redistribution. Nevertheless, the present bulk-rock data do not allow the magnitude or timing of REE redistribution within phosphate phases to be quantified. Accordingly, the observed association between REE and phosphate phases is interpreted as a mineralogical control on REE distribution rather than as independent evidence for a specific diagenetic mechanism.

The positive correlation between ΣREE and Y (r = 0.83) (Figure 6d) is consistent with broadly similar behavior of Y and the REE, particularly the HREE [72]. However, the Y/Ho ratios of 23.89–30.38 (average: 26.84 ± 2.31) are substantially lower than those commonly reported for open-ocean seawater (44–74) [3,19,73]. This difference indicates that the bulk-rock REE+Y system does not preserve an unmodified seawater signature. The relatively low Y/Ho ratios may reflect the combined influence of detrital and phosphate-bearing phases, adsorption and redistribution associated with the non-carbonate minerals, and limited post-depositional water–rock interaction [3,16,23,70].

The evidence for preservation of primary marine characteristics is therefore considered to be selective rather than complete. The broadly similar Al_2O_3-normalized REE patterns indicate that the principal relative REE distribution is internally consistent among the studied samples despite differences in absolute REE concentrations. The relatively coherent normalized REE patterns and the systematic associations among relatively immobile elements suggest that some features of the depositional geochemical environment may have been retained. However, these observations do not demonstrate complete preservation of the primary seawater signal. Recent Cretaceous paleoenvironmental studies likewise emphasize the importance of integrating multiple geochemical indicators when evaluating depositional redox conditions and paleoenvironmental evolution rather than relying on a single proxy [74,75].

In particular, the potential mobility of U during post-depositional alteration and the relatively low U/Th ratios (0.04–0.11; average: 0.07 ± 0.02) indicate that U/Th should be considered only as supporting evidence for predominantly oxic conditions rather than as a definitive indicator of redox state or preservation [76]. The relatively low V/Cr ratios (0.77–1.90; average: 1.18 ± 0.37) provide an additional, independent line of geochemical evidence compatible with predominantly oxic depositional conditions [76]. Nonetheless, V and Cr distributions in bulk-rock carbonates may also be influenced by detrital input, mineralogical controls, and post-depositional processes. The V/Cr ratio is likewise regarded as a complementary rather than definitive redox proxy [16,23,56,74,77]. Accordingly, the combined U/Th and V/Cr evidence supports, though not independently, relatively oxic depositional conditions.

Taken together, the REE distribution in the studied limestones reflects the combined influence of four principal processes: (1) input of REE-bearing siliciclastic materials; (2) concentration and fixation of REE in phosphate phases, particularly apatite; (3) dilution of bulk-rock REE concentrations by carbonate accumulation; and (4) limited redistribution during post-depositional processes. The strong ΣREE–Al_2O_3 relationship and the broadly consistent Al_2O_3-normalized REE patterns further indicate that the carbonate–non-carbonate mixing is an important control on absolute REE abundances, but that the observed relative REE fractionation cannot be attributed to the dilution alone. Consequently, the REE+Y system should not be interpreted as an unmodified record of Cretaceous seawater. Instead, it represents a partially modified carbonate geochemical archive in which some marine characteristics may have been retained, but whose interpretation requires integration of normalized REE patterns, Al_2O_3-normalized REE patterns, Y/Ho ratios, Ce and Eu anomalies, U/Th, V/Cr, mineralogical evidence, and indicators of detrital and phosphate contributions.

5.3. LREE–HREE Fractionation and Implications for Cretaceous Seawater Chemistry

The LREE–HREE fractionation provides an additional constraint on REE sources as well as on the extent to which marine geochemical characteristics may have been retained in carbonate rocks. However, this parameter can be influenced simultaneously by primary depositional processes, detrital input, variations in carbonate–non-carbonate proportions, and diagenetic modification and should therefore be interpreted cautiously. Modern seawater commonly exhibits relative HREE enrichment because HREE form stable complexes with carbonate and organic ligands and consequently behave more conservatively than LREE [3,11,22,25].

In the studied limestones, the values of $(La/Yb)_N$ and $(Nd/Yb)_N$ range from 1.35 to 1.89 (average: 1.63 ± 0.13) and 1.19 to 1.67 (average: 1.46 ± 0.16), respectively. The average $(La/Yb)_N$ values are higher than those reported for carbonate sediments from the Indian Ocean (0.93 ± 0.17) and Arabian Sea (0.98 ± 0.03) [63,78], but are comparable to values reported for shallow-marine carbonates (1.82 ± 0.46) [79] (Table 5). Similarly, the average $(Nd/Yb)_N$ values are higher than those reported for carbonate sediments from the Indian Ocean (0.83 ± 0.05) and Arabian Sea (0.85 ± 0.17) [63,78] and are close to those reported for shallow-marine carbonates (1.51 ± 0.30) [79].

Table 5. Values of certain geochemical parameters calculated for the studied limestones at Amir–Abad compared with the corresponding values of other sources like normal seawater, shallow marine carbonates, shallow marine limestones, Arabian Sea carbonate sediments, and Indian Ocean carbonate sediments.

	Amir–Abad Limestones (This Study)	**Seawater**	**Shallow Marine Carbonate [79]**	**Shallow Marine Limestone [65]**	**Arabian Sea Carbonate Sediments [73]**	**Indian Ocean Carbonate Sediments [78]**
REE (ppm)	42.35 ± 9.40	-	73 ± 20	32.2 ± 13.3	78 ± 40	-
Er/Nd	0.07 ± 0.01	0.27 [18]	0.07 ± 0.02	0.15 ± 0.03	0.11 ± 0.02	-
Y/Ho	26.84 ± 2.31	~44–74 [19]	-	38.13 ± 21.35	34.14 ± 1.64	-
$(La/Yb)_N$	1.63 ± 0.13	0.2–0.5 [11]	1.82 ± 0.46	0.732 ± 0.12	0.98 ± 0.03	0.93 ± 0.17
$(Nd/Yb)_N$	1.46 ± 0.16	0.205–0.497 [66]	1.51 ± 0.30	0.64 ± 0.08	0.85 ± 0.17	0.83 ± 0.13
Ce/Ce*	0.85± 0.06	<0.1–0.4 [11]	0.76 ± 0.16	0.57 ± 0.08	0.84 ± 0.06	0.56
Eu/Eu*	1.70 ± 0.18	-	0.58 ± 0.11	1.51 ± 0.64	1.15 ± 0.08	>1

The relatively elevated $(La/Yb)_N$ and $(Nd/Yb)_N$ ratios indicate weak enrichment of LREE relative to HREE. Although this pattern differs from the idealized HREE-enriched signature of open-ocean seawater, the degree of fractionation is relatively limited, and the PAAS-normalized patterns remain comparatively flat (Figure 6). Importantly, the broadly similar Al_2O_3-normalized REE patterns among the studied samples (Figure 7) indicate that the observed LREE–HREE relationship is not simply a consequence of differences in the absolute abundance of the non-carbonate fraction. Rather, carbonate dilution appears to have primarily affected the absolute REE concentrations, whereas the relative LREE–HREE distribution was additionally influenced by the composition of the REE-bearing non-carbonate components. The observed distribution therefore appears to represent a modified marine carbonate signal rather than a direct record of seawater composition.

The relative enrichment of LREE may partly reflect the contribution of siliciclastic materials. Kaolinite, plagioclase, hematite, and goethite of terrigenous origin can preferentially accommodate or transport LREE relative to HREE. Consequently, even a relatively small contribution of these minerals may increase the bulk-rock LREE/HREE ratios [65,66]. This interpretation is consistent with the positive relationships between ΣREE and Al_2O_3, SiO_2, Th, and Zr, which indicate that variations in the non-carbonate fraction contributed to the bulk-rock REE inventory. However, because the Al_2O_3-normalized patterns remain broadly similar among the samples, the LREE enrichment cannot be attributed solely to carbonate dilution and more likely reflects the composition and behavior of the REE-bearing non-carbonate fraction.

The Er/Nd ratio provides an additional measure of LREE–HREE fractionation. The Er/Nd ratios range from 0.06 to 0.08 (Table 3), indicating relatively consistent fractionation among the studied samples. Although these values are substantially lower than those of modern seawater [18], they are compatible with values reported for several marine carbonate rocks affected by variable detrital input and early diagenetic modification [16,23]. The low Er/Nd values therefore indicate modification of the REE system relative to modern seawater but do not necessarily imply complete loss of marine affinity.

Taken together, the LREE–HREE ratios and normalized REE patterns indicate that the studied limestones preserve a relatively coherent but modified REE signature. The available evidence suggests that carbonate dilution mainly influenced the absolute abundance of REEs, whereas the weak LREE enrichment and LREE–HREE fractionation were more likely related to the composition of the non-carbonate, particularly siliciclastic and phosphate-bearing components and to limited post-depositional redistribution. Accordingly, LREE–HREE fractionation should be interpreted as one component of a multi-proxy assessment of the Cretaceous marine geochemical environment.

5.4. Ce and Eu Anomalies: Implications for Redox Conditions, Terrigenous Input, and Diagenetic Modification

The Ce and Eu anomalies provide complementary information on depositional redox conditions, non-carbonate input, and post-depositional modification. In the studied samples, Ce/Ce* values range from 0.76 to 0.94 (average: 0.85 ± 0.06), indicating weak negative Ce anomalies. Negative Ce anomalies are generally compatible with relatively oxidizing conditions in marine depositional environments; however, their magnitude may also be affected by detrital input, phosphate-bearing phases, variations in the relative proportions of carbonate and non-carbonate components, and post-depositional processes [1,3,17,70]. Accordingly, the Ce anomalies are not interpreted here as direct evidence of an unmodified seawater signal, but rather as a geochemical feature whose depositional significance must be evaluated in conjunction with other independent proxies.

The Pr/Pr* values range from 0.93 to 1.13 and are generally close to unity. This relationship supports the interpretation that the observed negative Ce anomalies are unlikely to

result primarily from anomalous La behavior [3]. The Ce/Ce* versus Pr/Pr* plot (Figure 9) further indicates that most samples exhibit negative Ce anomalies that are not readily explained by La enrichment.

The relatively low Mn/Sr values (0.48–1.01) suggest that the studied limestones experienced limited to moderate diagenetic modification; however, Mn/Sr alone cannot establish the preservation of primary REE signatures. Therefore, the interpretation of Ce anomalies was evaluated using additional mineralogical and geochemical evidence rather than relying solely on Mn/Sr. In particular, the weak correlation between Ce/Ce* and U (r = 0.13) (Figure 10a) does not provide evidence for a direct relationship between Ce variability and U enrichment. Since U can be mobile during diagenesis, the absence of a Ce/Ce*–U correlation alone cannot be considered as sufficient evidence for the preservation of a primary Ce signal. Thus, the observed Ce anomalies may retain a component of the original marine redox signal, but their preservation should be regarded as tentative rather than demonstrated.

To further evaluate the redox interpretation, the U/Th ratio was considered as a complementary geochemical indicator. The calculated U/Th ratios range from 0.04 to 0.11, with an average of 0.07 ± 0.02 (Table 3). These relatively low U/Th values are consistent with predominantly oxic to relatively oxidizing depositional conditions. Nevertheless, because U may be remobilized during diagenesis and the present study is based on bulk-rock data, U/Th is regarded only as supporting evidence rather than a definitive redox proxy. Thus, the combined evidence from negative Ce anomalies, Pr/Pr* values close to unity, and relatively low U/Th ratios supports a relatively oxidizing marine depositional environment, although the extent to which these features record primary depositional conditions cannot be independently resolved from the present dataset.

The absence of significant correlations between Ce/Ce* and CaO (r = 0.18) (Figure 10b), Fe_2O_3 (r = 0.00) (Figure 10c), and MnO (r = 0.00) (Figure 10d) provides no clear evidence that variations in Ce anomalies were principally associated with the abundance of Fe–Mn oxides/hydroxides or the carbonate component. Similarly, the lack of a significant Ce/Ce*–CaO relationship suggests that carbonate dilution did not exert a direct, first-order control on the magnitude of the Ce anomaly. Nevertheless, these relationships cannot independently exclude diagenetic modification because Fe–Mn phases may occur at concentrations below the level required to generate a strong bulk-rock correlation, and REE redistribution may occur without producing simple element–element relationships [16,23,26,70].

In contrast, the positive correlations of Ce/Ce* with Th (r = 0.89) (Figure 10e), Y (r = 0.88) (Figure 10f), and Zr (r = 0.73) (Figure 10g) indicate that variations in Ce anomalies were associated, at least partly, with the non-carbonate component. The strong positive correlation between ΣREE and Ce/Ce* (r = 0.84) (Figure 10h) further indicates that the magnitude of the Ce anomaly is related to the overall REE inventory. Because ΣREE itself shows a positive relationship with Al_2O_3 (r = 0.55), these relationships suggest that variations in the non-carbonate fraction influenced both absolute REE concentrations and the magnitude of the observed Ce anomalies. However, this association does not demonstrate that detrital materials directly generated the negative Ce anomalies. Because ΣREE is itself influenced by detrital and phosphate-bearing phases, this relationship cannot be interpreted uniquely as evidence for either primary seawater control or diagenetic redistribution. Instead, these correlations indicate that variability in the non-carbonate fraction contributed substantially to the observed range of Ce anomalies.

The positive relationship between $(La/Sm)_N$ and Ce/Ce* (r = 0.80) (Figure 10i) further indicates an association between Ce-anomaly variability and REE fractionation. Collectively, these relationships suggest that the negative Ce anomaly is compatible with relatively oxidizing marine depositional conditions, but its magnitude was variably modified by

detrital input, phosphate phases, and differences in the relative abundance of the carbonate and non-carbonate materials, and potentially early diagenetic processes [23].

The Eu/Eu* values range from 1.44 to 1.98, with an average of 1.70 ± 0.18, indicating pronounced positive Eu anomalies. Several processes may generate positive Eu anomalies in carbonate rocks, including hydrothermal fluids, feldspar-bearing detrital material, reducing conditions, and diagenetic fluid–rock interaction [78,80–86]. Therefore, the positive Eu anomalies cannot be assigned uniquely to a single process by the present bulk-rock dataset.

Potential analytical effects related to Ba interference were also considered. The negative relationships between Eu/Eu* and Ba/Nd (r = −0.63) (Figure 11a) and Ba/Sm (r = −0.65) (Figure 11b), together with the absence of a significant positive correlation between Eu/Eu* and Ba (r = 0.15) (Figure 11c), do not support a major Ba-related control on the observed Eu anomalies [86].

Positive Eu anomalies in carbonate rocks can also be associated with hydrothermal activity. However, the studied limestones show no independent mineralogical or geochemical evidence for significant hydrothermal alteration, such as a hydrothermal mineral assemblage or pronounced Fe–Mn enrichment. Nonetheless, because fluid-inclusion, stable-isotope, and cathodoluminescence data were not obtained in the present study, a minor contribution from hydrothermal or diagenetic fluids cannot be completely excluded. Therefore, a significant hydrothermal origin for the positive Eu anomalies is not supported by the available evidence, although a minor contribution from later fluid–rock interaction cannot be definitively ruled out [26,74].

The possible contribution of detrital feldspar was evaluated using the Eu/Eu* versus Na_2O/Al_2O_3 relationship (Figure 11i). The absence of a positive relationship does not support a dominant control of plagioclase on the observed Eu anomalies [84,87–90]. Nevertheless, since plagioclase was detected as a minor/accessory mineral phase by XRD, a limited contribution from feldspar-bearing detrital materials cannot be completely disregarded.

In contrast, Eu/Eu* shows positive correlations with ΣREE (r = 0.75) (Figure 11d), Ce/Ce* (r = 0.93) (Figure 11e), Th (r = 0.91) (Figure 11f), Y (r = 0.89) (Figure 11g), and Zr (r = 0.67) (Figure 11h). These relationships indicate that Eu variability is associated with the overall REE inventory and with the non-carbonate component. The positive Eu/Eu*–ΣREE relationship, together with the strong association of ΣREE with Al_2O_3, further suggests that variations in the abundance of the REE-bearing non-carbonate fraction contributed to the observed variability in Eu anomalies. However, this relationship should not be interpreted as evidence that carbonate dilution itself generated the positive Eu anomaly. These correlations do not uniquely demonstrate a diagenetic origin for the positive Eu anomalies. Considering the identified phosphate phases, the association of Eu with non-carbonate components, and the absence of independent evidence for significant hydrothermal alteration, the positive Eu anomalies are best regarded as the result of multiple potentially overlapping controls, including phosphate-related mineralogical effects, limited detrital input, and possible redistribution during early diagenesis and/or fluid–rock interaction. The relative contribution of these processes cannot be quantitatively distinguished using the present dataset [23,70].

Overall, the contrasting behavior of Ce and Eu indicates that the two anomalies record different combinations of depositional and post-depositional processes. The negative Ce anomalies are compatible with relatively oxidizing marine depositional conditions and may retain a component of the primary marine redox signal, as also supported by Pr/Pr* values close to unity and relatively low U/Th ratios. However, this interpretation remains tentative because U may be mobile during diagenesis, while the magnitude of the Ce anomaly appears to have been influenced by detrital and phosphate-bearing components and variations in the relative abundance of carbonate and non-carbonate material, and po-

tentially by subsequent diagenetic processes. The positive Eu anomalies, in contrast, appear to reflect a combination of mineralogical and non-carbonate controls together with possible limited diagenetic redistribution. Consequently, reconstruction of the paleoenvironmental conditions of the Tizkuh Formation should rely on a multi-proxy approach integrating Ce and Eu anomalies, normalized REE patterns, Al_2O_3-normalized REE patterns, Y/Ho ratios, U/Th and other redox-sensitive elemental relationships, indicators of clastic contamination, and mineralogical evidence rather than on any single geochemical index [16,23,26,70].

5.5. Conceptual Model for the Geochemical Evolution of the Tizkuh Carbonate Platform

Based on the integrated mineralogical and geochemical evidence, the geochemical characteristics of the Tizkuh Formation limestones are interpreted to be more as the result of interaction among carbonate production, variable detrital input, phosphate-related REE accumulation, and subsequent diagenetic modification rather than representing an entirely pristine record of the Cretaceous seawater. The studied limestones constitute a mixed and partially modified geochemical archive in which selected primary depositional and redox-related features may have been retained. Accordingly, interpretation of the geochemical evolution of the carbonate platform requires simultaneous consideration of the original sedimentary components, depositional conditions, and post-depositional processes [14,16,23,26].

During the initial stage, sedimentation on a shallow carbonate platform, together with carbonate production and accumulation, resulted in the deposition of calcite-dominated limestones. The dominance of calcite, high CaO/MgO ratios, and the relatively low abundance of dolomite indicate that the studied succession was primarily carbonate-rich and did not experience pervasive dolomitization. Nevertheless, variable but generally limited input of siliciclastic and Fe-bearing materials from adjacent continental sources contributed quartz, clay minerals, hematite, goethite, and minor plagioclase to the depositional system. The presence of non-carbonate components are reflected by the negative relationships between CaO and several immobile and lithophile elements and also by the positive associations among SiO_2, Al_2O_3, TiO_2, Zr, Nb, Ta, Ga, Rb, and Cs. The inverse relationships between CaO and several non-carbonate-associated elements, together with the positive correlation between ΣREE and Al_2O_3 ($r = 0.55$), further indicate that variations in the relative proportion of the carbonate and non-carbonate materials exerted a dilution control on the absolute concentrations of the REE and other non-carbonate-associated elements.

The detrital component also contributed to the REE budget of the limestones. The positive relationships of ΣREE with SiO_2, Th, Zr, and Y indicate that the siliciclastic materials were important contributors and/or carriers of REE. The relatively low Y/Ho ratios and limited LREE–HREE fractionation further indicate that the REE system does not represent an unmodified seawater signature. Instead, the normalized REE patterns likely record the combined influence of the marine carbonate component and variable contributions from non-carbonate materials. Importantly, the broadly similar Al-normalized REE patterns among the studied samples (Figure 7) indicate that differences in absolute REE concentrations were partly related to variations in carbonate versus non-carbonate proportions, whereas the relative REE distribution pattern remained comparatively coherent. Thus, carbonate dilution appears to have modified REE abundances without being solely responsible for the observed REE fractionation.

Phosphate mineral phases represent another important control on the REE inventory. The strong positive correlation between ΣREE and P_2O_5, together with the occurrence of fine apatite crystals observed by SEM–EDS, indicates that phosphate-bearing phases were important repositories for REE in at least part of the studied limestones. Apatite can accommodate REE^{3+} through substitution for Ca^{2+} in its crystal structure and may therefore

contribute substantially to REE fixation and redistribution in carbonate sediments [68–70]. However, the available mineralogical and textural observations are insufficient to determine unequivocally whether the observed apatite is entirely authigenic, detrital, or partly diagenetic. Its contribution is therefore interpreted conservatively as a phosphate-related control on the REE budget rather than as definitive evidence for in situ or authigenic phosphate mineralization.

Following deposition and burial, the carbonate sediments underwent limited to moderate diagenetic modification. The Mn/Sr ratios, CaO/MgO ratios, mineralogical characteristics, and REE data collectively indicate that calcite recrystallization and redistribution of some mobile elements may have occurred, but there is no evidence for pervasive dolomitization or significant hydrothermal alteration. The relatively restricted range of Mn/Sr values and the preservation of coherent relationships among several relatively immobile elements suggest that diagenetic modification was not sufficiently intense to completely reorganize the whole-rock geochemical system. Nevertheless, the low Y/Ho ratios, positive Eu anomalies, and relationships between Ce/Ce*, Eu/Eu*, and non-carbonate indicators demonstrate that the REE system experienced some degree of post-depositional modification.

The different behavior of Ce and Eu provides additional constraints on this modification. The negative Ce anomalies, together with Pr/Pr* values close to unity and relatively low U/Th ratios, are compatible with relatively oxidizing depositional conditions and suggest that a component of the primary marine redox signal may have been retained. However, this interpretation remains tentative because U may be mobile during diagenesis, while the relationships between Ce/Ce* and Th, Zr, Y, and ΣREE indicate that the magnitude of the Ce anomaly was also influenced by the non-carbonate component. Therefore, the negative Ce anomalies are regarded as compatible with an oxidizing marine depositional environment rather than as unequivocal evidence of a pristine seawater redox signal. Similarly, the positive Eu anomalies cannot be uniquely attributed to early diagenetic redistribution because Eu variability may reflect coupled mineralogical, detrital, phosphate-related, and diagenetic controls. Thus, Ce and Eu anomalies should be regarded as complementary but differently sensitive indicators of the depositional and post-depositional history of the limestones.

Overall, the geochemical evolution of the Tizkuh carbonate platform can therefore be envisaged as a multistage process involving: (1) dominant carbonate production and accumulation on a shallow-marine platform, resulting in dilution of the concentrations of elements preferentially associated with the non-carbonate fraction; (2) variable incorporation of siliciclastic and Fe-bearing materials from adjacent continental sources; (3) incorporation and fixation of REE in phosphate-bearing phases, together with contributions from detrital minerals; and (4) subsequent recrystallization and limited water–rock interaction during early to moderate diagenesis. The relative importance of these processes varied among the studied samples and resulted in a geochemical system in which primary marine characteristics were partly retained but variably modified. The Al-normalized REE patterns provide an additional constraint on this model by showing that carbonate dilution affected absolute REE abundances, whereas the broadly coherent REE distribution patterns persisted after normalization to a non-carbonate-associated element.

Consequently, the Tizkuh Formation limestones should be considered a mixed and partially modified geochemical archive rather than a pristine record of the Cretaceous seawater. Nevertheless, the preservation of relatively coherent normalized REE patterns, weak negative Ce anomalies, and systematic relationships among REE and mineralogical indicators suggests that useful information concerning the depositional environment and aspects of the Cretaceous marine redox regime may still be extracted from these rocks. However, the extent to which these features represent primary depositional conditions

cannot be established conclusively from the present bulk-rock dataset. Such interpretations should therefore rely on a multi-proxy framework integrating REE patterns, Ce and Eu anomalies, Y/Ho ratios, U/Th, detrital indicators, major- and trace-element relationships, mineralogical evidence, Al-normalized REE patterns, and diagenetic proxies rather than on any single geochemical parameter [14,16,23,26,70].

A limitation of the present study is the relatively low sampling density in relation to the total thickness of the exposed Tizkuh Formation. The 15 analyzed samples were selected to represent the principal limestone intervals and lithological variability recognized along the studied profile. Therefore, the dataset is suitable for evaluating the overall mineralogical and geochemical characteristics of the sampled limestone intervals, but it does not permit reconstruction of continuous or high-resolution vertical geochemical variations throughout the entire 440 m-thick succession. Further high-density sampling would be required to investigate, on a smaller scale, stratigraphic variations in mineralogical composition and elemental concentrations in greater detail.

6. Conclusions

1. Geochemical and mineralogical data indicate that the chemical composition of the Tizkuh Formation limestones was controlled primarily by three interacting processes: carbonate production and accumulation, variable input of siliciclastic materials, and limited to moderate post-depositional modification. Variations in the relative proportions of the carbonate and non-carbonate components appear to have been an important control on whole-rock geochemical variability. The systematic decrease in the bulk-rock concentrations of many non-carbonate-associated elements with increasing CaO is consistent with a carbonate dilution effect, whereby increasing carbonate accumulation lowers the apparent concentrations of elements predominantly associated with the non-carbonate fraction. The siliciclastic component additionally contributed to the variability of several lithophile and relatively immobile trace elements. However, the available bulk-rock data do not permit individual elements to be assigned unequivocally to specific mineral hosts.
2. The REE distribution was controlled by the combined effects of carbonate dilution, siliciclastic input, and phosphate-bearing phases. The studied limestones were not anomalously enriched in REEs, with ΣREE concentrations being broadly within the range of those reported for marine carbonate rocks. The positive correlations of ΣREE with SiO_2, Th, Zr, and Y indicate an important contribution of the non-carbonate fraction to the bulk-rock REE inventory, whereas the negative ΣREE–CaO relationship is consistent with carbonate dilution. In addition, the strong positive relationship between ΣREE and P_2O_5, together with the occurrence of apatite identified by SEM–EDS in two selected samples, indicates that phosphate-bearing phases exerted an important mineralogical control on REE distribution in at least part of the succession. These relationships suggest that phosphate mineral phases may have contributed to REE fixation and/or subsequent redistribution; however, the limited SEM–EDS observations do not permit the abundance or quantitative importance of apatite to be generalized to the entire succession.
3. The REE fractionation patterns indicate that the bulk-rock REE system does not represent an unmodified primary seawater signature. The limited LREE enrichment relative to HREE is likely related to the combined influence of siliciclastic input, phosphate-bearing phases, and post-depositional redistribution. The relatively low Y/Ho ratios further indicate modification of the REE system relative to open-marine seawater. Nevertheless, the broadly coherent normalized REE patterns and overall REE characteristics remain compatible with deposition in a marine carbonate setting.

Thus, the REE data are best regarded as a partially modified carbonate geochemical archive rather than a direct record of contemporaneous seawater composition.

4. The weak negative Ce anomalies and Pr/Pr* values close to unity are compatible with relatively oxidizing marine depositional conditions, but their preservation as primary seawater signals remains tentative. The relatively low U/Th ratios (0.04–0.11; average: 0.07 ± 0.02) and V/Cr ratios (0.77–1.90; average: 1.18 ± 0.37) provide additional, but not definitive, support for predominantly oxic conditions. The weak Ce/Ce*–U relationship (r = 0.13), together with the potential mobility of U during diagenesis, does not provide a robust independent test of Ce preservation. Moreover, the relationships of Ce/Ce* with Th, Y, Zr, ΣREE, and $(La/Sm)_N$ indicate that the magnitude of the Ce anomaly was influenced, at least partly, by the non-carbonate and REE-bearing components. The positive Eu anomalies are likewise interpreted cautiously and may reflect a combination of mineralogical controls, limited detrital feldspar contribution, phosphate-related effects, and possible early diagenetic and/or fluid–rock redistribution. The present bulk-rock dataset does not permit the relative contribution of these processes to be quantitatively distinguished.
5. Overall, the Tizkuh Formation limestones represent a mixed and partially modified carbonate geochemical archive formed along the southern margin of the Neo-Tethys. Although their bulk-rock REE+Y composition cannot be considered an unmodified record of Cretaceous seawater, selected geochemical characteristics—particularly the weak negative Ce anomalies—remain compatible with relatively oxidizing marine depositional conditions. Consequently, paleoenvironmental reconstruction should rely on a multi-proxy approach integrating REE distribution and fractionation patterns, Ce and Eu anomalies, Y/Ho ratios, U/Th, V/Cr and other redox-sensitive elemental relationships, detrital and phosphate indicators, geochemical correlations, and mineralogical evidence, while explicitly considering carbonate dilution, siliciclastic input, and post-depositional modification. Finally, the relatively low sampling density limits reconstruction of continuous, high-resolution vertical geochemical variations throughout the 440 m-thick succession; therefore, densely spaced sampling would be required to resolve short-scale stratigraphic variability.

Author Contributions: Conceptualization, A.A.; methodology, A.A. and A.A.C.; software, A.A. and A.S.; validation, A.A. and A.A.C.; formal analysis, A.A. and N.K.; investigation, A.A.; resources, A.A.; data curation, A.A. and N.K.; writing—original draft preparation, A.A. and A.A.C.; writing—review and editing, A.A. and A.A.C.; visualization, A.A. and A.S.; supervision, A.A.; project administration, A.A. and A.S.; funding acquisition, A.S. All authors have read and agreed to the published version of the manuscript.

Funding: This research was funded by Firat University grant number MF 26.138 project.

Data Availability Statement: Data are contained within the article.

Conflicts of Interest: The authors declare no conflicts of interest.

References

1. German, C.R.; Elderfield, H. Application of the Ce anomaly as a paleoredox indicator: The ground rules. *Paleoceanography* **1990**, *5*, 823–833. [CrossRef]
2. Bau, M. Rare-earth element mobility during hydrothermal and metamorphic fluid-rock interaction and the significance of the oxidation state of europium. *Chem. Geol.* **1991**, *93*, 219–230. [CrossRef]
3. Bau, M.; Dulski, P. Distribution of yttrium and rare earth elements in the Penge and Kuruman Iron Formations, Transvaal Supergroup (South Africa): Precambrian seawater signatures versus post-depositional modification. *Precambrian Res.* **1996**, *79*, 37–55.

4. Evans, D.; Gray, W.R.; Rae, J.W.B.; Greenop, R.; Webb, P.B.; Penkman, K.; Kröger, R.; Allison, N. Trace and major element incorporation into amorphous calcium carbonate (ACC) precipitated from seawater. *Geochim. Cosmochim. Acta* **2020**, *290*, 293–311. [CrossRef]
5. Liu, X.M.; Hardisty, D.S.; Lyons, T.W.; Swart, P.K. Evaluating the fidelity of the cerium paleoredox tracer during variable carbonate diagenesis on the Great Bahamas Bank. *Geochim. Cosmochim. Acta* **2019**, *248*, 25–42. [CrossRef]
6. Mehrabi, H.; Yahyaei, E.; Navidtalab, A.; Rahimpour-Bonab, H.; Abbasi, R.; Omidvar, M.; Assadi, A.; Honarmand, J. Depositional and diagenetic controls on reservoir properties along the shallow-marine carbonates of the Sarvak Formation, Zagros Basin: Petrographic, petrophysical, and geochemical evidence. *Sediment. Geol.* **2023**, *454*, 106457. [CrossRef]
7. Abedini, A.; Calagari, A.A.; Sasmaz, A. Geochemical characteristics, REE distribution, and Eu-Ce anomalies in limestones of the Triassic Elika Formation, Shahindezh district, NW Iran: Insights into paleoenvironment. *J. Afr. Earth Sci.* **2026**, *244*, 106333. [CrossRef]
8. Zhao, Y.; Wei, W.; Li, S.; Yang, T.; Zhang, R.; Somerville, I.D.; Santosh, M.; Wei, H.; Wu, J.; Yang, J.; et al. Rare earth element geochemistry of carbonates as a proxy for deep-time environmental reconstruction. *Palaeogeogr. Palaeoclimatol. Palaeoecol.* **2021**, *574*, 110443. [CrossRef]
9. Zhang, K.; Shields, G.A. Early diagenetic mobilization of rare earth elements and implications for the Ce anomaly as a redox proxy. *Chem. Geol.* **2023**, *635*, 121619. [CrossRef]
10. Paquette, J.; Reeder, R.J. Relationship between surface structure, growth mechanism, and trace element incorporation in calcite. *Geochim. Cosmochim. Acta* **1995**, *59*, 735–749. [CrossRef]
11. Elderfield, H.; Greaves, M.J. The rare earth elements in seawater. *Nature* **1982**, *296*, 214–219. [CrossRef]
12. Smrzka, D.; Zwicker, J.; Klaucke, I.; Himmler, T.; Bohrmann, H.; Peckmann, J. Trace elements in methane-seep carbonates: Potentials, limitations, and perspectives. *Earth-Sci. Rev.* **2020**, *208*, 103263. [CrossRef]
13. Abedini, A.; Khosravi, M. Geochemical constraints on the Triassic–Jurassic Amir-Abad karst-type bauxite deposit, NW Iran. *J. Geochem. Explor.* **2020**, *211*, 106489. [CrossRef]
14. Webb, G.E.; Kamber, B.S. Rare earth elements in Holocene reefal microbialites: A new shallow seawater proxy. *Geochim. Cosmochim. Acta* **2000**, *64*, 1557–1565. [CrossRef]
15. Hoskin, P.W.O.; Schaltegger, U. The composition of zircon and igneous and metamorphic petrogenesis. *Rev. Mineral. Geochem.* **2003**, *53*, 27–62. [CrossRef]
16. Nothdurft, L.D.; Webb, G.E.; Kamber, B.S. Rare earth element geochemistry of Late Devonian reefal carbonates, Canning Basin, Western Australia: Confirmation of a seawater REE proxy in ancient limestones. *Geochim. Cosmochim. Acta* **2004**, *68*, 263–283. [CrossRef]
17. Lawrence, M.G.; Greig, A.; Collerson, K.D.; Kamber, B.S. Rare earth element and yttrium variability in South East Queensland waterways. *Aquat. Geochem.* **2006**, *12*, 39–72. [CrossRef]
18. de Baar, H.J.W.; German, C.R.; Elderfield, H.; van Gaans, P. Rare earth element distributions in anoxic waters of the Cariaco Trench. *Geochim. Cosmochim. Acta* **1988**, *52*, 1203–1219. [CrossRef]
19. Bau, M.; Koschinsky, A.; Dulski, P.; Hein, J.R. Comparison of the partitioning behaviours of yttrium, rare earth elements, and titanium between hydrogenetic marine ferromanganese crusts and seawater. *Geochim. Cosmochim. Acta* **1996**, *60*, 1709–1725. [CrossRef]
20. Bellanca, A.; Masetti, D.; Neri, R. Rare earth elements in limestone–marlstone couplets: Paleoenvironmental sensitivity. *Chem. Geol.* **1997**, *141*, 141–152. [CrossRef]
21. Sholkovitz, E.R.; Landing, W.M.; Lewis, B.L. Ocean particle chemistry: The fractionation of rare earth elements between suspended particles and seawater. *Geochim. Cosmochim. Acta* **1994**, *58*, 1567–1579. [CrossRef]
22. Nozaki, Y. Rare earth elements and their isotopes in the ocean. In *Encyclopedia of Ocean Sciences*; Academic Press: London, UK, 2001; pp. 2354–2366.
23. Zhao, Y.; Wei, W.; Santosh, M.; Hu, J.; Wei, H.; Yang, J.; Liu, S.; Zhang, G.; Yang, D.; Li, S. A review of retrieving pristine rare earth element signatures from carbonates. *Palaeogeogr. Palaeoclimatol. Palaeoecol.* **2022**, *586*, 110765. [CrossRef]
24. Singh, A.; Singh, B.P.; Kanhaiya, S.; Quasim, M.A.; Patra, A.; Singh, S.K.; Srivastava, V.K. Geochemistry of Palaeoproterozoic Kajrahat Limestone, Vindhyan Supergroup, central India: Insights into depositional conditions and sources of rare earth elements. *Carbonates Evaporites* **2024**, *39*, 30. [CrossRef]
25. Byrne, R.H.; Kim, K.-H. Rare earth element scavenging in seawater. *Geochim. Cosmochim. Acta* **1990**, *54*, 2645–2656. [CrossRef]
26. Frimmel, H.E. Trace element distribution in Neoproterozoic carbonates as palaeoenvironmental indicator. *Chem. Geol.* **2009**, *258*, 338–353. [CrossRef]
27. Hood, A.V.S.; Planavsky, N.J.; Wallace, M.W.; Wang, X. The effects of diagenesis on geochemical paleoredox proxies in sedimentary carbonates. *Geochim. Cosmochim. Acta* **2018**, *232*, 265–287. [CrossRef]
28. Taylor, S.R.; McLennan, S.M. *The Continental Crust: Its Composition and Evolution*; Blackwell Scientific Publications: Oxford, UK, 1985; 312p.

29. Bau, M.; Alexander, B. Preservation of primary REE patterns without Ce anomaly during dolomitization of Mid-Paleoproterozoic limestone and the potential re-establishment of marine anoxia immediately after the "Great Oxidation Event". *S. Afr. J. Geol.* **2006**, *109*, 81–86. [CrossRef]
30. Webb, G.E.; Nothdurft, L.D.; Kamber, B.S.; Kloprogge, J.T.; Zhao, J.X. Rare earth element geochemistry of scleractinian coral skeleton during meteoric diagenesis: A sequence through neomorphism of aragonite to calcite. *Sedimentology* **2009**, *56*, 1433–1463. [CrossRef]
31. Madhavaraju, J.; González-León, C.M.; Lee, Y.I.; Armstrong-Altrin, J.S.; Reyes-Campero, L.M. Geochemistry of the Mural Formation (Aptian–Albian) of the Bisbee Group, Northern Sonora, Mexico. *Cretac. Res.* **2010**, *31*, 400–414. [CrossRef]
32. Liang, T.; Jones, B. Characteristics of primary rare earth elements and yttrium in carbonate rocks from the Mesoproterozoic Gaoyuzhuang Formation, North China: Implications for the depositional system. *Sediment. Geol.* **2021**, *426*, 105864. [CrossRef]
33. Abedini, A.; Calagari, A.A. Rare earth element geochemistry of the Upper Permian limestone: The Kanigorgeh mining district, NW Iran. *Turk. J. Earth Sci.* **2015**, *24*, 365–382. [CrossRef]
34. Chen, J.; Algeo, T.J.; Zhao, L.; Chen, Z.Q.; Cao, L.; Zhang, L.; Li, Y. Diagenetic uptake of rare earth elements by bioapatite, with an example from Lower Triassic conodonts of South China. *Earth-Sci. Rev.* **2015**, *149*, 181–202. [CrossRef]
35. Liu, J.; Song, J.; Yuan, H.; Li, X.; Li, N.; Duan, L. Rare earth element and yttrium geochemistry in sinking particles and sediments of the Jiaozhou Bay, North China: Potential proxy assessment for sediment resuspension. *Mar. Pollut. Bull.* **2019**, *144*, 79–91. [CrossRef] [PubMed]
36. Cao, C.; Liu, X.-M.; Chen, J. Cerium anomaly as a tracer for paleo-oceanic redox conditions: A thermodynamics-based Ce oxidation modeling approach. *Front. Earth Sci.* **2022**, *10*, 927826. [CrossRef]
37. Cengiz, O.; Kıray, D.; Özeğdemir, E. Petrography and Geochemistry of the Middle Jurassic–Lower Cretaceous Limestones from the Mustafakemalpaşa Quarries, Bursa, Turkey: The Depositional Environmental and Diagenetic Processes. *Minerals* **2025**, *15*, 1135. [CrossRef]
38. Wang, Y.D.; Huang, C.M.; Sun, B.N.; Quan, C.; Wu, J.Y.; Lin, Z.C. Paleo-CO_2 variation trends and the Cretaceous greenhouse climate. *Earth-Sci. Rev.* **2014**, *129*, 136–147. [CrossRef]
39. Haq, B.U. Cretaceous eustasy revisited. *Glob. Planet. Change* **2014**, *113*, 44–58. [CrossRef]
40. Li, Q.; Ding, F.; Ruhl, M.; Wang, Y.; Li, Y.; Yang, L.; Xu, K.; Xie, X. Geochemistry of the Lower Cretaceous limestones in the Eastern Tethys Gyabula Formation (Himalaya, southern Tibet): Implications for the depositional environment and tectonic setting. *Arab. J. Geosci.* **2021**, *14*, 2353. [CrossRef]
41. Alavi, M. Tectonics of the Zagros orogenic belt of Iran: New data and interpretations. *Tectonophysics* **1994**, *229*, 211–238. [CrossRef]
42. Stöcklin, J. Structural history and tectonics of Iran: A review. *AAPG Bull.* **1968**, *52*, 1229–1258. [CrossRef]
43. Alavi, M. Tectonostratigraphic synthesis and structural style of the Alborz mountain system in Northern Iran. *J. Geodyn.* **1996**, *21*, 1–33. [CrossRef]
44. Stampfli, G.M.; Borel, G.D. A plate tectonic model for the Paleozoic and Mesozoic constrained by dynamic plate boundaries and restored synthetic oceanic isochrons. *Earth Planet. Sci. Lett.* **2002**, *196*, 17–33. [CrossRef]
45. Berberian, M.; King, G.C.P. Towards a paleogeography and tectonic evolution of Iran. *Can. J. Earth Sci.* **1981**, *18*, 210–265. [CrossRef]
46. Brindley, G.W. Quantitative X-ray mineral analysis of clays. In *Crystal Structures of Clay Minerals and Their X-Ray Identification*; Brindley, G.W., Brown, G., Eds.; Mineralogical Society Monograph; Mineralogical Society: London, UK, 1980; Volume 5, pp. 411–438.
47. Moore, D.M.; Reynolds, R.C. *X-Ray Diffraction and the Identification and Analysis of Clay Minerals*; Oxford University Press: Oxford, UK, 1989.
48. Horowitz, A.J. *A Primer on Sediment–Trace Element Chemistry*, 2nd ed.; Lewis Publishers: Chelsea, MI, USA, 1991.
49. Zhao, M.Y.; Zheng, Y.F. Marine carbonate records of terrigenous input into Paleotethyan seawater: Geochemical constraints from Carboniferous limestones. *Geochim. Cosmochim. Acta* **2014**, *141*, 508–531. [CrossRef]
50. Augustsson, C.; Aehnelt, M.; Olivarius, M.; Voigt, T.; Gaupp, R.; Hilse, U. Provenance from the geochemical composition of terrestrial clastic deposits—A review with case study from the intracontinental Permo-Triassic of European Pangea. *Sediment. Geol.* **2023**, *456*, 106496. [CrossRef]
51. Qian, P.; Wu, Y.; Tian, Z.; Yang, L.; Zheng, X.; Luo, J. Provenance of the Xiashu loess in the lower reaches of the Yangtze River, China: A review. *Front. Earth Sci.* **2024**, *12*, 1426389. [CrossRef]
52. Cornell, R.M.; Schwertmann, U. *The Iron Oxides: Structure, Properties, Reactions, Occurrences and Uses*, 2nd ed.; Wiley-VCH: Weinheim, Germany, 2003.
53. Alloway, B.J. *Heavy Metals in Soils: Trace Metals and Metalloids in Soils and Their Bioavailability*, 3rd ed.; Springer: Dordrecht, The Netherlands, 2013.
54. Swart, P.K. The geochemistry of carbonate diagenesis: The past, present and future. *Sedimentology* **2015**, *62*, 1233–1304. [CrossRef]

55. Brand, U.; Veizer, J. Chemical diagenesis of a multicomponent carbonate system—1: Trace elements. *J. Sediment. Petrol.* **1980**, *50*, 1219–1236. [CrossRef]
56. Banner, J.L.; Hanson, G.N. Calculation of simultaneous isotopic and trace element variations during water-rock interaction with applications to carbonate diagenesis. *Geochim. Cosmochim. Acta* **1990**, *54*, 3123–3137. [CrossRef]
57. Banner, J.L. Application of the trace element and isotope geochemistry of strontium to studies of carbonate diagenesis. *Sedimentology* **1995**, *42*, 805–824. [CrossRef]
58. Fantle, M.S.; Barnes, B.D.; Lau, K.V. The role of diagenesis in shaping the geochemistry of the marine carbonate record. *Annu. Rev. Earth Planet. Sci.* **2020**, *48*, 549–583. [CrossRef]
59. Higgins, J.A.; Blättler, C.L.; Lundstrom, E.A.; Santiago-Ramos, D.P.; Akhtar, A.A.; Crüger Ahm, A.-S.; Bialik, O.; Holmden, C.; Bradbury, H.; Murray, S.T.; et al. Mineralogy, early marine diagenesis, and the chemistry of shallow-water carbonate sediments. *Geochim. Cosmochim. Acta* **2018**, *220*, 512–534. [CrossRef]
60. Kamber, B.S.; Webb, G.E. The geochemistry of late Archaean microbial carbonate: Implications for ocean chemistry and continental erosion history. *Geochim. Cosmochim. Acta* **2001**, *65*, 2509–2525. [CrossRef]
61. Tucker, M.E.; Wright, V.P. *Carbonate Sedimentology*; Blackwell Scientific Publications: Oxford, UK, 1990.
62. Flügel, E. *Microfacies of Carbonate Rocks: Analysis, Interpretation and Application*, 2nd ed.; Springer: Berlin/Heidelberg, Germany, 2010.
63. Nath, B.N.; Bau, M.; Rao, B.R.; Rao, C.M. Trace and rare earth elemental variation in Arabian Sea sediments through a transect across the oxygen minimum zone. *Geochim. Cosmochim. Acta* **1997**, *61*, 2375–2388. [CrossRef]
64. Nagarajan, R. Geochemistry and Depositional Environment of Neoproterozoic Sediments of Bhima Basin, Karnataka, South India. Ph.D. Thesis, Anna University, Chennai, India, 2003; 292p.
65. Cullers, R.L. Implications of elemental concentrations for provenance, redox conditions, and metamorphic studies of shales and limestones near Pueblo, CO, USA. *Chem. Geol.* **2002**, *191*, 305–327. [CrossRef]
66. Garzanti, E.; Resentini, A.; Andò, S.; Vezzoli, G.; Pereira, A.; Vermeesch, P. Physical controls on sand composition and relative durability of detrital minerals during ultra-long distance littoral and aeolian transport (Namibia and southern Angola). *Sedimentology* **2015**, *62*, 971–996. [CrossRef]
67. Rahim, H.U.; Haider, S.W.; Jamil, M.; Khalil, R.; Jan, J.A.; Yar, M. Lithofacies and geochemical analysis of the late Paleozoic Tobra Formation, Salt Range, Pakistan: Implications for the provenance and paleoenvironment reconstruction. *Russ. Geol. Geophys.* **2025**, *66*, 917–935. [CrossRef]
68. Reynard, B.; Lécuyer, C.; Grandjean, P. Crystal-chemical controls on rare-earth element concentrations in fossil biogenic apatites and implications for paleoenvironmental reconstructions. *Chem. Geol.* **1999**, *155*, 233–241. [CrossRef]
69. Filippelli, G.M. Phosphate rock formation and marine phosphorus geochemistry: The deep time perspective. *Chemosphere* **2011**, *84*, 759–766. [CrossRef] [PubMed]
70. Tostevin, R.; Shields, G.A.; Tarbuck, G.M.; He, T.; Clarkson, M.O.; Wood, R.A. Effective use of cerium anomalies as a redox proxy in carbonate-dominated marine settings. *Chem. Geol.* **2016**, *438*, 146–162. [CrossRef]
71. Caetano-Filho, S.; Paula-Santos, G.M.; Dias-Brito, D. Carbonate REE plus Y signatures from the restricted early marine phase of South Atlantic Ocean (late Aptian–Albian): The influence of early anoxic diagenesis on shale-normalized REE plus Y patterns of ancient carbonate rocks. *Palaeogeogr. Palaeoclimatol. Palaeoecol.* **2018**, *497*, 90–104.
72. Bau, M. Controls on the fractionation of isovalent trace elements in magmatic and aqueous systems: Evidence from Y/Ho, Zr/Hf, and lanthanide tetrad effect. *Contrib. Mineral. Petrol.* **1996**, *123*, 323–333. [CrossRef]
73. Nozaki, Y.; Zhang, J.; Amakawa, H. The fractionation between Y and Ho in the marine environment. *Earth Planet. Sci. Lett.* **1997**, *148*, 329–340. [CrossRef]
74. Bellefroid, E.J.; Planavsky, N.J.; Hood, A.V.S.; Halverson, G.P.; Spokas, K.; Reinhard, C.T. Constraints on Paleoproterozoic ocean chemistry from rare earth element patterns in marine carbonates. *Precambrian Res.* **2018**, *310*, 339–356.
75. Awan, R.S.; Liu, B.; Yasin, Q.; Wood, D.A.; Rahim, H.U.; Gul, M.A.; Ali, S.; Iltaf, K.H.; Khan, A. Paleoenvironmental conditions and key drivers of organic matter accumulation in the early Cretaceous Talhar shale, Lower Indus Basin, Pakistan. *J. Asian Earth Sci.* **2025**, *292*, 106716. [CrossRef]
76. Jones, B.; Manning, D.A.C. Comparison of geochemical indices used for the interpretation of palaeoredox conditions in ancient mudstones. *Chem. Geol.* **1994**, *111*, 111–129. [CrossRef]
77. Friese, A.; Derry, L.A.; Kah, L.C.; Turchyn, A.V.; Owens, J.; Planavsky, N.J. Controls on rare earth element signatures during carbonate diagenesis. *Geochim. Cosmochim. Acta* **2021**, *309*, 1–21.
78. Nath, B.N.; Roelandts, I.; Sudhakar, M.; Plüger, W.L. Rare earth element patterns of the Central Indian Basin sediments related to their lithology. *Geophys. Res. Lett.* **1992**, *19*, 1197–1200. [CrossRef]
79. Madhavaraju, J.; Ramasamy, S. Rare earth elements in limestones of Kallankurichchi Formation of Ariyalur Group, Tiruchirapalli Cretaceous, Tamil Nadu. *J. Geol. Soc. India* **1999**, *54*, 291–301. [CrossRef]

80. Shields, G.; Stille, P. Diagenetic constraints on the use of cerium anomalies as palaeoseawater redox proxies: An isotopic and REE study of Cambrian phosphorites. *Chem. Geol.* **2001**, *175*, 29–48. [CrossRef]
81. Alexander, B.W.; Bau, M.; Andersson, P.; Dulski, P. Continentally-derived solutes in shallow Archean seawater: Rare earth element and Nd isotope evidence in iron formation from the 2.9 Ga Pongola Supergroup, South Africa. *Geochim. Cosmochim. Acta* **2008**, *72*, 378–394. [CrossRef]
82. Auer, G.; Reuter, M.; Hauzenberger, C.A.; Piller, W.E. The impact of transport processes on rare earth element patterns in marine authigenic and biogenic phosphates. *Geochim. Cosmochim. Acta* **2017**, *203*, 140–156. [CrossRef]
83. Zhu, B.; Ge, L.; Yang, T.; Jiang, S.; Lv, X. Stable isotopes and rare earth element compositions of ancient cold seep carbonates from Enza River, northern Apennines (Italy): Implications for fluid sources and carbonate chimney growth. *Mar. Pet. Geol.* **2019**, *109*, 434–448. [CrossRef]
84. Murray, R.W.; Buchholtz ten Brink, M.R.; Gerlach, D.C.; Russ, G.P.; Jones, D.L. Rare earth, major, and trace elements in chert from the Franciscan Complex and Monterey Group, California: Assessing REE sources to fine-grained marine sediments. *Geochim. Cosmochim. Acta* **1991**, *55*, 1875–1895. [CrossRef]
85. Madhavaraju, J.; Lee, Y.I. Geochemistry of the Dalmiapuram Formation of the Uttatur Group (Early Cretaceous), Cauvery basin, southeastern India: Implications on provenance and paleo-redox conditions. *Rev. Mex. Cienc. Geol.* **2009**, *26*, 380–394.
86. Jiang, S.Y.; Zhao, H.X.; Chen, Y.Q.; Yang, J.H.; Ling, H.F. Trace and rare earth element geochemistry of carbonate rocks: Effect of barium interference on europium anomalies determined by ICP-MS. *Chem. Geol.* **2007**, *243*, 250–267.
87. Alibo, D.S.; Nozaki, Y. Rare earth elements in seawater: Particle association, shale-normalization, and Ce oxidation. *Geochim. Cosmochim. Acta* **1999**, *63*, 363–372. [CrossRef]
88. Özyurt, M.; Kırmacı, M.Z.; Al-Aasm, I.; Hollis, C.; Taslı, K.; Kandemir, R. REE characteristics of Lower Cretaceous limestone succession in Gümüşhane, NE Turkey: Implications for ocean paleoredox conditions and diagenetic alteration. *Minerals* **2020**, *10*, 683. [CrossRef]
89. Murray, R.W.; Buchholtz ten Brink, M.R.; Brumsack, H.J.; Gerlach, D.C.; Russ, G.P., III. Rare earth elements in Japan Sea sediments and diagenetic behavior of Ce/Ce: Results from ODP Leg 127. *Geochim. Cosmochim. Acta* **1991**, *55*, 2453–2466. [CrossRef]
90. Nagarajan, R.; Madhavaraju, J.; Armstrong-Altrin, J.S.; Nagendra, R. Geochemistry of Neoproterozoic limestones of the Shahabad Formation, Bhima Basin, Karnataka, southern India. *Geosci. J.* **2011**, *15*, 9–25. [CrossRef]

Disclaimer/Publisher's Note: The statements, opinions and data contained in all publications are solely those of the individual author(s) and contributor(s) and not of MDPI and/or the editor(s). MDPI and/or the editor(s) disclaim responsibility for any injury to people or property resulting from any ideas, methods, instructions or products referred to in the content.